# Manuscript Details

| | |
|---|---|
| **Manuscript number** | SG_2019_445_R1 |
| **Title** | Shear localisation, strain partitioning and frictional melting in a debris avalanche generated by volcanic flank-collapse |
| **Article type** | Original article |


**Abstract**

The Arequipa volcanic landslide deposit to the east of Arequipa (Peru) originated from the Pichu Pichu volcanic complex, covering an area >100 km2. The debris avalanche deposit exhibits internal flow structures and basal pseudotachylytes. We present field, microstructural and chemical observations from slip surfaces below and within the deposit which show varying degrees of strain localisation. At one locality the basal shear zone is localised to a 1-2 cm thick, extremely sheared layer of mixed ultracataclasite and pseudotachylyte containing fragments of earlier frictional melts. Rheological modelling indicates brittle fragmentation of the melt may have occurred due to high strain rates, at velocities of >31 m.s-1 and that frictional melting is unlikely to provide a mechanism for basal lubrication. Elsewhere, we observe a <40 cm thick basal shear zone, overprinted by sub-parallel faults that truncate topological asperities to localise strain. We also observe shear zones within the avalanche deposit, suggesting that strain was partitioned. In conclusion, we find that deformation mechanisms fluctuated between cataclasis and frictional melting during emplacement of the volcanic debris avalanche; exhibiting strain partitioning and variable shear localisation, which, along with underlying topography, changed the resistance to flow and impacted runout distance.



| | |
|---|---|
| **Keywords** | Sector collapse; Pseudotachylyte; Strain partitioning; Shear localisation; Cataclasis |



| | |
|---|---|
| **Corresponding Author** | Amy Hughes |
| **Corresponding Author's Institution** | University of Liverpool |
| **Order of Authors** | Amy Hughes, Jackie E. Kendrick, Guido Salas, Paul Wallace, François Legros, Giulio Di Toro, Yan Lavallee |


| | |
|---|---|
| **Suggested reviewers** | Christie Rowe, Benjamin van Wyk de Vries, James Kirkpatrick, Emily Brodsky, William Griffith |

## Submission Files Included in this PDF

**File Name [File Type]**

Hughes et al - Resubmission Letter.docx [Cover Letter]

Hughes et al - Response to comments.docx [Response to Reviewers]

Hughes et al Manuscript - revised track changes.docx [Response to Reviewers]

Hughes et al Figures - track changes.docx [Response to Reviewers]

Hughes et al Highlights.docx [Highlights]

Hughes et al Manuscript - revised.docx [Manuscript File]

Hughes et al Figures - no track changes.docx [Figure]

Hughes et al declaration-of-competing-interests.docx [Conflict of Interest]

Hughes et al. - Author statement.docx [Author Statement]

Hughes et al - Supplementary material.docx [Supplementary Material]

## Submission Files Not Included in this PDF

**File Name [File Type]**

Hughes et al. - Supplementary data.xlsx [Supplementary Material]

**Highlights**

- Pichu Pichu collapsed resulting in a debris avalanche that propagated >27 km.
- Shear localisation varies with extreme examples resulting in frictional melting.
- Secondary slip surfaces within the deposit show delocalisation of shear from base.
- Shear resistance due to basal pseudotachylytes calculated.
- We estimate that flow velocity exceeded 31 $m.s^{-1}$.

# Shear localisation, strain partitioning and frictional melting in a debris avalanche generated by volcanic flank-collapse

**Amy Hughes[a], Jackie E. Kendrick[a], Guido Salas[b], Paul A. Wallace[a], François Legros[c], Giulio Di Toro[d] and Yan Lavallée[a]**

**Corresponding Author: Amy Hughes**

[a] *Department of Earth, Ocean and Ecological Sciences, University of Liverpool, Liverpool L69 3GP, United Kingdom.*

[b] *Department of Geology and Geophysical Sciences, National University of San Agustin. Arequipa, Peru*

[c] *Freelance researcher, Arequipa, Peru*

[d] *Department of Geoscience, University of Padova, Via Gradenigo, 6 - 35131 Padova*

## Abstract

The Arequipa volcanic landslide deposit to the east of Arequipa (Peru) originated from the Pichu Pichu volcanic complex, covering an area >100 km$^2$. The debris avalanche deposit exhibits internal flow structures and basal pseudotachylytes. We present field, microstructural and chemical observations from slip surfaces below and within the deposit which show varying degrees of strain localisation. At one locality the basal shear zone is localised to a 1-2 cm thick, extremely sheared layer of mixed ultracataclasite and pseudotachylyte containing fragments of earlier frictional melts. Rheological modelling indicates brittle fragmentation of the melt may have occurred due to high strain rates, at velocities of >31 m.s$^{-1}$ and that frictional melting is unlikely to provide a mechanism for basal lubrication. Elsewhere, we observe a <40 cm thick basal shear zone, overprinted by sub-parallel faults that truncate topological asperities to localise strain. We also observe shear zones within the avalanche deposit, suggesting that strain was partitioned. In

conclusion, we find that deformation mechanisms fluctuated between cataclasis and frictional melting during emplacement of the volcanic debris avalanche; exhibiting strain partitioning and variable shear localisation, which, along with underlying topography, changed the resistance to flow and impacted runout distance.

**Keywords**

Sector collapse; Pseudotachylyte; Strain partitioning; Shear localisation; Cataclasis

## 1. Introduction

Volcanic edifices are inherently unstable structures formed by the superimposition of layers of varying volcanic materials on relatively rapid geological timescales (Voight, 2000; Acocella and Puglisi, 2010). Structural instability of volcanoes and other orogenic landforms can be prompted by a range of factors such as: magma intrusion e.g., Mount St. Helens (Lipman and Mullineaux, 1981); overloading of flanks (Swanson et al., 1976), tectonic stresses (Lagmay et al., 2000), ground motion during earthquakes (Voight and Elsworth, 1997), hydrothermal activity (Day, 1996; Voight and Elsworth, 1997), alteration (Reid, 2004), precipitation (McGuire, 1996), freeze-thaw (Kawamura and Miura, 2013), and erosion (McGuire, 1996). This is combined with a natural variability in coherency, porosity, crystallinity and glass content of materials, which affects the strength and primary deformation mode (e.g., brittle vs ductile) of the edifice-forming rocks (e.g. Heap et al., 2010; Benson et al., 2012). Collapses of unstable volcanic structures occur at a wide range of scales, the smallest examples form from shallow slope instability events (Cecchi et al., 2004) and rockfalls (Calder et al., 2002), whereas larger scale instabilities can produce deep-seated slip events that may subject magmatic systems to decompression that trigger unrest and even eruptions (e.g. Hunt et al., 2018).

Large-scale collapse landslides pose significant hazards to life and property within the spatial range of the event (e.g. Siebert, 1992). Quantifying the potential distance these collapses may travel, the rate at which onset occurs and the speed of the avalanche itself as it propagates from the source area is therefore paramount in hazard risk assessments. Large landslide volumes can exceed $10^9$ $m^3$ (Siebert, 1984) and travel at speeds up to 100 $m.s^{-1}$ (Siebert et al., 1987; Shea and van Wyk de Vries, 2008) and those with volumes in excess of $10^6$ $m^3$ often exhibit anomalously high mobility (Scheidegger, 1973). Mobility considers a combination of velocity and runout distance from source (Iverson et al., 2015), which can often be greater than ten times the height of fall (the elevation change from source to final position of the mass of material) in these instances (Legros, 2002). Analysis of the ratio of height of fall to runout distance against volume of landslides highlights that landslides with larger volumes travel longer distances, suggesting the importance of a mechanism that acts to lower frictional coefficients, allowing them to be more mobile than predicted by simple frictional sliding models (Shea and van Wyk de Vries, 2008). Such behaviour has been identified in events developing in all rock types (Legros, 2002 and references therein), suggesting a commonality of the process. Several mechanisms to reduce frictional coefficients during frictional sliding of landslides have been put forth, including: mechanical fluidisation (Davies, 1982; Campbell et al., 1995), the lubricating effects of basal groundwater or ice (Lucchitta, 1987; Legros, 2002; De Blasio, 2011), trapped air (Shreve, 1968), salt (De Blasio, 2011), acoustic fluidisation (Melosh, 1979, 1986; Johnson et al., 2016), mechanical and thermal fluid pressurisation (e.g. Ferri et al., 2011) elastohydrodynamic lubrication (Brodsky and Kanamori, 2001), frictional velocity weakening (e.g. Wang et al., 2017) and the formation of a lubricating frictional melt layer (Legros et al., 2000; De Blasio and Elverhøi, 2008; Wang et al., 2017).

The production of frictional melts is the result of frictional heating due to strain localisation onto a discrete, thin slipping layer (Sibson, 1975). These frictional melts are then preserved in the

77 geological record as pseudotachylytes, and are usually ascribed to seismogenic fault activity
78 (Sibson, 1975, 1977; Spray, 1992; Shimamoto and Lin, 1994; Di Toro et al., 2006; Nielsen et al.,
79 2008), volcanic conduit shear zones (e.g. Kendrick et al., 2012), and at the base of some mass
80 movements (Erismann, 1979; Masch et al., 1985; Legros et al., 2000; Lin et al., 2001; Hacker et
81 al., 2014; Bernard and van Wyk de Vries, 2017). The presence of frictional melts along fault slip
82 zones has often been suggested to act as a lubricant (Di Toro et al., 2006); yet, they may conversely
83 act as a viscous brake (Fialko and Khazan, 2005), especially in intermediate and felsic volcanic
84 rocks sheared at low (<10 MPa) normal stresses or low lithostatic loads (Lavallée et al., 2012;
85 Kendrick et al., 2014). Importantly, the transient physico-chemical evolution of frictional melt
86 during slip impacts rheological evolution (Lin and Shimamoto, 1998; Wallace et al., 2019), which
87 controls slip velocity, shear resistance and any thermo-mechanical feedback due to viscous energy
88 dissipation (Nielsen et al., 2010) that, in the case of mass movements, may ultimately regulate the
89 runout distance.

90 Careful examination of the internal structures of mass movement deposits, such as large
91 landslides (including debris avalanches), suggests a spectrum of behaviour; from those which
92 disaggregate during transport to those transported over long distances whilst maintaining their
93 coherence, exhibited by undisturbed structures such as discrete lithological units and intrusions
94 (Glicken, 1998; Erismann and Abele, 2001; Hacker et al., 2014). Some evidence suggests that
95 larger events have preserved their internal structures (Erismann and Abele, 2001; De Blasio and
96 Elverhøi, 2008). In order to preserve these features, shear must have been localised to a relatively
97 narrow layer to prevent wholescale deformation. Shear localisation is an integral part of flow
98 segregation and means that the basal mechanisms of debris avalanches and volcanic collapses
99 largely control emplacement. On this layer, shear rates (and thus frictional heating) may be
100 extremely high as a result of the high velocity of the mass movement (De Blasio and Elverhøi,
101 2008). Pseudotachylytes have only been identified at the base of a few landslides, including:

Kofels, Austria (Erismann, 1979); Langtang, Nepal (Masch et al., 1985); Tsaoling, Taiwan (Lin et al., 2001); Markagunt slide, Utah (Hacker et al., 2014), Sevier slide, Utah (Biek et al., 2019), French Massif Central (Bernard and van Wyk de Vries, 2017) and Arequipa, Peru (Legros et al., 2000). The Arequipa volcanic landslide deposit displays a rare example of preserved pseudotachylyte at the base of a landslide originating from a volcanic source, namely Pichu Pichu volcano. The internal structure of the deposit is exposed owing to multiple incisions by rivers since emplacement >1 Ma ago (Legros et al., 2000). Here we present new observations from an extensive geological survey of the Arequipa volcanic landslide deposit, including re-examination of the original outcrops investigated in Legros et al. (2000) as well as newly identified shear exposures.

## 2. Geological background

Pichu Pichu is part of the modern Central Andean Volcanic Zone and is located along the NE margin of the Arequipa basin, 30 km to the east of the city of Arequipa (Fig. 1). The volcanic arc trends approximately NW-SE, associated with major regional sinistral strike-slip faults trending NW-SE (de Silva and Francis, 1990; Lavallée et al., 2009). The Arequipa basin is filled with four distinct, high-K calc-alkaline ignimbrites commonly referred to as the "Sillar" (Lebti et al., 2006). These range in age from the 13.19 ± 0.09 Ma Rio Chili Ignimbrite to the 1.03 ± 0.09 Ma Yura Tuff (Lebti et al., 2006). The source of these ignimbrites has been inferred to evidence a relict volcanic caldera now buried by the construction of Chachani volcanic complex during the quaternary (in the last 1 Ma to 642 ka; Aguilar et al., 2016). Similarly, the ignimbrites underlie the younger Arequipa volcanic landslide deposit (Legros et al., 2000; Lebti et al., 2006) estimated to have occurred at ~1 Ma (Lebti et al., 2006).

125 Pichu Pichu itself is an extinct volcanic complex with andesitic lava flows dated to 6.71 ±
126 0.57 Ma using K-Ar dating (Kaneoka and Guevara, 1984) with no evidence of younger activity.
127 The collapse of a significant portion of the volcanic flank resulted in the formation of an open
128 arcuate ridge morphology, facing the large volcanic debris avalanche deposit found to the east of
129 Arequipa (Fig. 1). Initially the deposit was mapped to extend to the NE of Arequipa, however
130 further investigation of those deposits found that the chemistry of entrained lava blocks and flow
131 package characteristics more closely correlate to lava flows from an earlier cone of El Misti that
132 underwent collapse before the formation of the modern day cone (Thouret et al., 2001). These
133 more recent flows partially overlie and obscure the older collapse deposits now interpreted to
134 originate from Pichu Pichu. More recently the northern boundary of the debris flow deposit was
135 re-mapped in the area of Chiguata to follow the break in slope between the flank of El Misti and
136 the irregular topography identified as the Pichu Pichu collapse formation (Thouret et al., 2001).
137 The debris avalanche deposit has been stated to evidence both mixed and block facies using
138 nomenclature of Glicken (1991), and has a basal pseudotachylyte (Legros et al., 2000), but has not
139 been mapped in detail (Thouret et al., 2001).

140

141 **3. Methods**

142 The debris avalanche deposit was surveyed in 2017. Topographic maps were used to
143 identify valleys and gullies that would be potential sites for basal exposures using the relative
144 altitudes from the previously identified basal contact (Legros et al., 2000) at 2600 m above sea
145 level. Where basal contacts were located, we also examined the debris avalanche deposit above
146 for internal flow features.

147 Samples were collected from several localities; for basal contacts samples were generally
148 taken from above, below and within the shear zone. For all samples, flow direction was noted

149 (determined from the position from source, clast imbrication and striations if present) in the field
150 and ascribed to each specimen to enable structural analysis. Orientated, polished thin sections were
151 used for both microtextural and geochemical analyses. Backscattered electron images (BSE) used
152 for microtextural analysis were taken on a Phillips XL30 scanning electron microscope (SEM) at
153 the University of Liverpool with 20 kV accelerating voltage and 10 μm working distance.

154 Bulk chemistry was determined by X-ray fluorescence (XRF) at the University of Leicester
155 using a PANalytical Axios Advanced XRF Spectrometer. Major element analyses were
156 determined from glass beads fused from ignited powders and trace elements on pressed powder
157 pellets. Relative precision and accuracy were better than 1.5 % for major elements and 5 % for
158 trace elements based on a series of repeat analyses on reference materials (Bardon Hill
159 granodiorite and Whin Sill dolerite; see supplementary materials).

160 The geochemical compositions of phases in the underlying ignimbrite, pseudotachylytes,
161 cataclasites and lithic clasts from within the debris avalanche were measured using a Cameca
162 SX100 electron probe micro-analyser (EPMA) at the University of Manchester, using wavelength
163 dispersive spectroscopy (WDS). Calibration of the detectors were conducted on a range of
164 standards (albite for Si and Na, wollastonite for Ca, fayalite for Fe, corundum for Al, ilmenite for
165 Ti, periclase for Mg, tephrite for Mn and potassium feldspar for K). These standards were revisited
166 at the start of each working day, although the albite standard and the VG568 rhyolite glass standard
167 (Yellowstone National Park, Wyoming) were revisited regularly during analyses and before and
168 after each sample to ensure there was no drift. Measurements on crystals were conducted with a
169 focused ~1 μm beam with 20 nA current and 15 kV accelerating voltage. Analyses conducted on
170 pseudotachylyte and interstitial glass in lithic clasts were conducted using a defocused 10 μm
171 beam with 5 nA current and 15 kV accelerating voltage. Additionally, a defocused beam was also
172 used to sample the bulk chemistry of areas of ultracataclasite. All tests with both focused and
173 defocused beam had peak count times of 20 seconds and background (off peak) of 10 seconds.

In an attempt to obtain accurate and precise glass chemistries and minimise potential contamination from common restites (surviving crystals) in the pseudotachylyte glass, a 5 μm beam was also used for 6 analyses; they were found to return similar totals and chemistries to analyses done with the 10 μm beam.

In order to perform a rheological analysis of the frictional melt, the chemical composition obtained by EPMA was used as input in the GRD viscosity calculator (Giordano et al., 2008). ImageJ (Schneider et al., 2012) was employed to analyse phases in BSE images and estimate the crystal fraction as well as a maximum packing fraction, calculated following Mueller et al. (2010) and Klein et al. (2017). This data was input into the empirical relative viscosity calculator of Costa et al. (2009) to compute the rheology of the frictional melt suspensions.

## 4. Results

### 4.1. Field Observations

During our field campaign, we surveyed the Arequipa volcanic landslide deposit and closely examined key structures. The deposit is characterised by a heavily eroded area of high topography extending 26 km west from Pichu Pichu in a broad, fan-like shape (Fig. 1). The upper surface of the deposit is draped by fall deposits of more recent volcanic activity in the area. Legros et al. (2000) originally estimated the volume of the deposit to be >10 $km^3$, however, with the deposit covering over 200 $km^2$ and thicknesses observed at >100 m even at distances >20 km from the source, the volume could exceed even 20 $km^3$. Outcrops of the basal contact suggest a gentle 5$^o$ average slope of the original underlying topography. Current topography indicates that the central section of the deposit exceeds 300 m in thickness. An accurate estimation of the volume in this case is impossible due to the unknown basal topography, erosion of the deposit, poor mapping of the distal extent and a number of overlying fall deposits.

198 (Insert Fig. 1 here)

199 The deposit is cut by multiple rivers and their tributaries, including the Rio Socabaya in
200 which localities 2 and 3 are found (Fig. 1). Locality 1 is situated in a different river-cutting near
201 the Characato District. These incisions expose some of the internal flow structures developed
202 during the debris avalanche. Here, we describe observations of key structures from three localities
203 with extensive exposure. These include basal contacts, defining the paleotopography, as well as
204 mid-body shear zones and clastic dykes.

205

206 **4.1.1. Locality 1 – Basal pseudotachylyte**

207 Originally, the base of the debris avalanche deposit was observed in a river-cutting near
208 Characato District to the SE of Arequipa (Legros et al., 2000), approximately 24 km from Pichu
209 Pichu (Loc.1 see Fig.1). Here, the exposure presented by the river-cut is approximately 75 m long
210 and 10 m high approximately parallel to the expected transport direction (Fig. 2a-b). Although the
211 deposit extends further in all directions, vegetation covers most of the rocks on shallow
212 topography. In this locality, the debris avalanche deposit is rather massive, made of a white-grey,
213 granular medium consisting primarily of ash- and lapilli-size clasts of andesite lithics and
214 individual crystals (Fig. 2a-b). The andesite blocks are porphyritic, containing 20 % plagioclase
215 (up to 2.2 mm) and 15.3 % amphibole phenocrysts (up to 2 mm) with microlite-rich groundmass.
216 The andesite blocks occasionally reach 30 cm in size within the deposit and often display jigsaw
217 brecciation fracture patterns.

218 (Insert Fig. 2 here)

219 The underlying ignimbrite is exposed as a poorly consolidated and highly weathered rock
220 of pale grey colour consisting of ash-sized grains without large lapilli. Crystals of both biotite and
221 plagioclase are identifiable alongside dark lithic fragments but all are rarely larger than 1 mm in

size. The rock is highly fractured and contains non-continuous veins of silicic hydrothermal material up to 1 cm thick (Fig. 2c-d). These veins all follow a similar orientation, striking in a 014-020 direction with high dip angles of 80-90$^{o}$ to the east, following the orientation of regional tectonic features (Lebti et al., 2006).

The contact between the debris deposit and the underlying basal ignimbrite is sharp, consisting of a thin, dark grey, vitreous layer approximately 1-1.5 cm thick (Fig 2c-d). The contact is observed at an elevation of 2610-2620 m in the northern face of the river-cutting and is dipping away from the outcrop face towards the north (strike 090 and 091) at variable angles, but generally around 35º(Fig. 2a-b). The contact visibly extends over a length of ca. 60 m and is curvilinear, increasing in elevation by approximately 4-5 m over a distance of approximately 10 m away from Pichu Pichu at this locality. Over-hanging areas of the upper slip surface at the base of the deposit exhibit striations trending 286 degrees which deviates approximately 25 degrees north from the expected flow direction. The material either side of the contact is highly brecciated, containing no fragments larger than 4 cm within 50 cm of the contact.

#### 4.1.2. Locality 1 – Intra-body shear zone

Strain localisation was not restricted to the basal contact at Loc. 1. An additional shear zone was identified within the deposit, some 20 m above the basal contact at 2636 m elevation and 30 m due NE from the basal contact previously described. Here, a change in colour is noted above and below the shear zone. The lower unit is a pale grey colour, fine-grained breccia, similar to that described directly above the basal contact but with rare larger (>20 cm) andesitic blocks. Above is a breccia with red-coloured matrix, rich in andesitic blocks (Fig. 2e-f). The clasts in this upper lithology are larger, up to 50 cm, with less jigsaw brecciation and more angular shapes. These two units are separated by a layer of light brown material with no large clasts that varies from 2- 10 cm thick and which is seen to inject into the lithology above. Within this, there is a thin

246 layer of dark, microcrystalline material, approximately 3-4 mm thick (Fig. 2e-f). The shear zone
247 is observed to extend laterally for approximately 45 m and runs sub-parallel to the basal contact
248 below at a strike of 108 degrees dipping to the north by ~20º.

249

250 **4.1.3. Locality 2 – Cataclastic basal contact**

251 A new exposure of the deposit base was found to the northeast of the original locality in a
252 different river valley, approximately 17.5 km from Pichu Pichu (Loc. 2 see Fig. 1). Here, the
253 materials forming the debris avalanche deposit and the underlying ignimbrite remain the same as
254 in Loc. 1, yet the upper surface of the ignimbrite is, in some laterally discontinuous sections,
255 draped by a 1-2 m thick layer of more clay rich, lahar deposit material with some imbrication of
256 small clasts. The nature of the contact is however different and varies laterally within the outcrop,
257 which totals approximately 300 m along a river-cutting (Fig. 3). The contact, observed at an
258 elevation of 2854 to 2858 m, is seen in the north face of the river-cutting, near-parallel to the flow
259 direction and is generally linear and almost horizontal (Fig. 3a-b). It is largely visible as a sharp
260 boundary between the two units (with either the thin lahar layer or ignimbrite as the lower unit).
261 A large clast is preserved near the base of the debris avalanche, cut by multiple well-defined
262 fractures parallel to the primary contact (Fig. 3c-d). In this locality, no vitreous layer is present,
263 but the shear zone contains extremely fragmented, fine, angular material and displays red iron
264 oxide stains and 303º trending striations on the lower contact surface with the lahar (Fig. 3c-d).
265 This is a more northerly direction of flow, due to the fanning of the deposit across the land surface.

266 (Insert Fig. 3 here)

267 140 m to the west, separated from the previously described outcrop by an area of
268 vegetation, an undulating contact is visible between the debris flow and the ignimbrite material
269 where troughs were present in the paleotopography (i.e., the upper surface of the ignimbrite; Fig.

3e-f). The deposit filled the depression and exhibits diffusely distributed alignment of material (akin to inclined sub-parallel laminations) up to a sharp slip surface that crosscuts the debris avalanche deposit (Fig. 3e-f). Here, the base of a >2 m large andesitic clast is flat and parallel to the primary slip surface, showing signs of a throughgoing, bisecting rupture. No vitreous layer is present in the shear zone at this locality.

#### 4.1.4. Locality 3 – Intra-body shear zone and clastic dykes

In the Rio Socabaya gorge (Loc. 3 see Fig. 1), river incision exposes a >800 m long, up to 100 m high section of the debris avalanche deposit on both sides of the river valley. Here, the deposit is made of a massive, white-grey, granular medium consisting primarily of ash- and lapilli-size clasts of andesite lithics and crystals. However, in this locality, rare larger blocks of andesite were observed in the deposit up to 3-4 m in size. There is no visible basal contact between the facies identified, though the ignimbrite is exposed approximately 200 m to the west. Instead, the main rock mass exhibits multiple clastic dykes as well as intra-body shear zones some 5-10 m above the river bottom. The structurally-lowest shear zone, identified at the western end of the southern bank, developed within the main body of rock and does not separate disparate units within the debris avalanche deposit (Fig. 4). The shear zone appears as a linear feature marked by a thin, microcrystalline layer some 0.5 cm thick and extending over a length of approximately 5 m. The layer is not straight, but rather undulose. There is no discernible variation in clast shape or size in relation to the shear zone, though it is often obscured by vegetation. A few metres to the west of the end of the visible shear zone there is a clastic dyke, 2 m thick and >10 m high intruding sub-vertically into the deposit.

(Insert Fig. 4 here)

293 Multiple clastic dykes have been injected into the debris deposit from below, though the
294 source of the material is not observed in the field. These structures range in size from 10 cm to
295 2-3 m in thickness and reach up to several tens of metres in length (Fig. 5a-b). The thickness of
296 the larger clastic dykes changes along their length, generally tapering towards their tips. Most of
297 the dykes are sub-vertical, but there are several occurrences of sections of dykes, locally projecting
298 horizontally around large, metre-scale clasts. The edges are sharp with the deposit, and material
299 entrained in the clastic dykes varies in size and prevalence. The majority of the dykes contain
300 predominantly fine-grained clastic material with small lithic clasts (mostly andesitic) and crystal
301 fragments. In one case, a dyke contained over 50 % mass of clasts (in a fine-grained groundmass),
302 varying in composition and 1-30 cm in size. The margins of this dyke are devoid of large clasts,
303 are fine-grained and show evidence of laminar shear banding (Fig. 5c-d). In other cases, the dykes
304 do not show evidence of internal strain localisation or gradational deposition. The dykes are intact
305 and do not exhibit any offset, anticipated from post-emplacement shear within the bulk of the
306 avalanche, indicative of their late stage occurrence.

307 (Insert Fig. 5 here)

308 A second site observed in the same river valley is a shear zone consisting of a near-planar
309 feature through the deposit exposed on the inside bend of the southern bank. This shear zone is
310 approximately 25 m in length, with no discernible variation in lithology on either side. There is an
311 observed reduction of the number of clasts above 3 cm in a layer 20 cm in thickness above the
312 planar feature (Fig. 6), though intermittent large clasts up to 50 cm in size are present. At this shear
313 zone the planar feature is additionally highlighted by its interaction with the clastic dykes. A dyke
314 propagating from below terminates at the shear zone, increasing in width from 1 m to 3 m at the
315 intersection, visible in the outcrop and extending several metres along the shear plane, gradually
316 pinching out. 3 m to the west of the large clastic dyke, another dyke, 30 cm in width cuts across
317 the planar shear zone into the unit above (Fig 6).

318 (Insert Fig. 6 here)

319

320 **4.2. Microstructural analysis**

321 Thin sections of sheared samples were made perpendicular to shear and parallel to the slip
322 vector. Micro-textural analysis was performed using optical microscopy and BSE imagery.

323

324 **4.2.1. Locality 1 – Pseudotachylyte basal contact**

325 Microtextural analysis of the basal contact at Loc. 1 reveals that the dark layer observed at
326 outcrop scale comprises a 12 mm thick vitreous layer with ~3 mm thick undulose, and diffuse
327 boundaries at the top and bottom to cataclasites, which contain lithic clasts of bounding lithologies
328 up to 2 mm in size (Fig. 7).

329 Visual observation of the central dark vitreous layer shows that it is made of a mix of
330 tortuous (fluidal) black isotropic filaments (in plane-polarised light), up to 0.7 mm thick and 5 mm
331 long, and a large fraction (around 40 %) of a dark brown material consisting of identifiable small
332 rock fragments and crystals (Fig. 7). SEM image analysis reveals the black isotropic filaments to
333 be bubble-bearing material with no identifiable crystal structure (Fig. 8). Later EPMA analysis
334 produced consistent chemistry, ruling out the presence of small crystals. Therefore, as identified
335 in Legros et al. (2000), the isotropic black material is interpreted to be glass, with interspersed
336 ultracataclastic, crystal-rich dark brown material. The glass filaments contain varying fractions of
337 vesicles (Fig. 8a-b) which are up to 8 μm in size and occasionally elongated in the direction of en-
338 echelon alignment of the melt filaments. Where preserved around large clasts, elongate vesicles
339 form trails following the direction of shearing. Within the filaments, small, rounded patches of
340 silica (5 μm) are observed.

341 (Insert Fig.7 here)

342 In the brown material the crystals are predominantly plagioclase feldspar up to 0.6 mm in
343 size with a modal size <0.4 mm. They show as equant fragments with multiple fractures.
344 Additionally, smaller pyroxene crystals and occasional hornblende (<0.1 mm) are observed but
345 are concentrated on the outer edges of the dark, vitreous layer. SEM image analysis reveals that
346 the larger clasts have extensive cracking (Fig. 8d) but remain together forming a brecciated
347 texture. The fractured and sheared plagioclase crystals (Fig. 8a & c) form elongate layers of
348 plagioclase-dominated fragments.

349 The layering between pseudotachylyte glass and ultracataclasite follows Riedel shear
350 bands concordant with the shear in the flow direction (Fig. 7). The darker, glass-rich filaments are
351 more predominant in the centre of the layer and are absent from the bounding cataclasite. In these
352 marginal cataclastic zones (separating glass layer from the andesite above and ignimbrite below),
353 we observed large clasts consisting of fragments of mixed vesicular pseudotachylyte-
354 ultracataclasite banded materials (pst in Fig 8e-f), similar in texture to the intact vitreous layer.
355 The fragments are further fractured (showing trivial offset) and the margins are sub-angular.

356 (Insert Fig. 8 here)

357

358 **4.2.2. Locality 1 – Intra-body shear surface**

359 The intra-body shear plane approximately 20 m above the basal contact at Loc. 1 is
360 dominated by the presence of clasts and microcrystalline material. The visibly pale layer in the
361 outcrop is a poorly sorted clast rich cataclasite, the dark vitreous layer is denser ultracataclasite
362 welded with small amounts of amorphous material between grain contacts (Fig. 9a). The largest
363 clasts observed here are andesitic, 5-6 mm in size and semi-rounded, which are larger than the
364 clasts near to the basal contact hosting frictional melt (section 4.2.1). Smaller crystal fragments,

365 primarily of plagioclase are also present (Fig. 9b). In addition, the contact between the cataclasite
366 and the thin, denser ultracataclasite layer is sharp (Fig. 9b-c).

367 (Insert Fig. 9 here)

368

369 **4.2.3. Locality 1 – Basal ignimbrite**

370 Analysis of the ignimbrite below the contact at Loc. 1 found that the formation is rich in
371 similar sized anhedral plagioclase and sanidine crystals, commonly 1-2 mm in size and up to 3
372 mm with occasional smaller quartz and biotite crystals up to a maximum of 1 mm in size (Fig.
373 10a). The plagioclase and sanidine crystals occasionally form glomerocrysts containing a
374 combination of the two most abundant phenocryst types. These crystals are hosted in a matrix of
375 small needle-shaped glass shards, (<0.5 mm). In the sample collected there is no evident welding
376 of the material, which has high porosity. The crystal assemblage matches that described for the La
377 Joya Ignimbrite formation mapped within the Arequipa basin infill, which is thought to extend
378 across the whole area below the debris avalanche deposit (Lebti et al., 2006).

379 (Insert Fig. 10 here)

380

381 **4.2.4. Locality 2 – Cataclastic basal contact**

382 From the basal contact at Locality 2, there is no evidence of the localisation of shear onto
383 a single zone. Instead, the material across a band of approximately 40 cm thickness is formed of
384 highly fractured lithic and crystalline fragments and clasts hosted in a matrix of clay (Fig. 10c)
385 with no evidence of glass. Larger lithic fragments, ranging in size from <1 mm up to 7-10 mm in
386 size, are identifiable as andesitic in composition with similar crystal content as clasts from Loc. 1,
387 with abundant sub-euhedral plagioclase (<1 mm) and subhedral amphibole phenocrysts (<0.8

388 mm). Plagioclase forms the largest of the crystalline fragments in the shear zone, though small,
389 subangular, amphibole and biotite crystals around 1 mm in size are also observed in the cataclasite.
390 Several large pumiceous clasts up to ~4 cm in size are also preserved within the shear zone with
391 only minor fracturing. These pumiceous clasts contain plagioclase, sanidine and biotite. Small
392 fragments are often monocrystalline, commonly plagioclase up to 2 mm in size. The orientation
393 of these fragments shows no evidence of Riedel shearing and there are no pervasive shear fabrics
394 observed within the cataclasite.

395

396 **4.2.5. Locality 3 - Clastic dyke**

397 A sample of a large clastic dyke in the northern face exposure at Loc. 3 is observed to
398 contain considerable fractured glassy pumice fragments, andesite clasts (up to 7 mm in thin section
399 though field observations indicate larger clasts are present), individual crystals of plagioclase and
400 a high clay content (Fig. 10b). Additionally, some biotite (tabular, up to 1 mm) is present, which
401 is not observed in the lithologies of the debris avalanche but is observed in the ignimbrite and
402 cataclastic basal shear zone.

403

404 **4.3. Geochemical analysis**

405 Geochemical analysis was performed to reconcile physico-chemical processes associated
406 with the evolution of shear and frictional melting. XRF analysis was used to constrain the chemical
407 composition of the host rocks, confirming the andesitic nature of the avalanche deposit and the
408 rhyolitic chemistry of the ignimbrite (Fig. 11, see supplementary data).

409 EPMA was conducted on several mineral phases from host rocks and crystal fragments
410 and amorphous areas from the basal layer at Loc. 1 to constrain the development of frictional

411 melting (with respect to the host lithologies). The plagioclase crystals in the vitreous layer as well
412 as in andesite lithics within the ultracataclasite and ignimbrite host wall rock are compositionally
413 grouped (Fig. 11), with CaO ranging from 6 to 9 wt.% and NaO from 6 to 8 wt.% (see
414 supplementary data). Amphibole crystals in lithic fragments as well as rare individual crystals in
415 the ultracataclasite at Loc. 1 were found to be compositionally similar and were absent in the
416 vitreous layer (Fig. 11, see supplementary data). The two types of pyroxene present in the andesite,
417 cataclasite and vitreous layer, were identified as augite (clinopyroxene; Ca-rich) and enstatite
418 (orthopyroxene; Mg-Fe rich).

419 (Insert Fig. 11 here)

420 Glasses in both the preserved vitreous layer and in a fragment of glass-bearing material
421 found in the cataclasite were analysed (Fig. 8). The EPMA chemical composition of glass from
422 the basal pseudotachylyte plots between the XRF bulk chemistry of the underlying ignimbrite and
423 the andesitic blocks from the debris avalanche deposit (Fig. 11). The glass however tends to be
424 enriched in $SiO_2$, plotting closer to the composition of the ignimbrite than that of the andesite. In
425 contrast, the glass fragments preserved in the marginal cataclasite of the basal shear zone spans a
426 wider range in chemistry that is notably more mafic in composition. The glass in these
427 pseudotachylyte fragments has less CaO wt.% and $SiO_2$ wt.% than either the andesite or the
428 ignimbrite (Fig. 11b). Analyses on the ultracataclasite within the layer returned poor totals with
429 highly varying chemistries, suggesting mixed lithology fragments.

430

431 **5. Interpretation**

432 The field, microstructural and geochemical data can be used to make several interpretations
433 about the mechanics of shearing within the debris avalanche.

434

435 **5.1. Intergranular forces and fragmentation**

436 The contrasting nature of the different basal shear zone exposures provide clues as to the
437 emplacement mechanisms. At the basal contact at Loc. 1, we do not observe large andesitic clasts
438 within 5 m of the contact and there is evidence of intense brecciation (Fig. 2). In comparison, at
439 Loc. 2 we observe a number of large andesitic clasts, up to metre scale in close proximity to the
440 basal shear localisation zone (Fig. 3). This suggests greater intergranular forces may have occurred
441 near the base of the flow at Loc. 1 compared to Loc. 2 that exceed the elastic limit of the clasts
442 (Davies and McSaveney, 2009), resulting in intense fracturing and reduction in clast and particle
443 sizes (Arabnia and Sklar, 2016). This qualitative observation can also be made at a smaller scale
444 within the shear localisation zone itself, where centimetre-scale clasts at Loc. 2 have survived (in
445 comparison to the smaller fragments in the glass-bearing layer at Loc. 1). Some of these fragments
446 are pumiceous (Fig. 10c) material that, due to their highly vesicular nature, would be mechanically
447 weaker than other crystalline and lithic fragments. Their survival means that there was less
448 cataclastic damage associated with this shear zone. The inferred greater intergranular forces at
449 Loc. 1 also enhances the ability for frictional heating (Carslaw and Jaeger, 1959) that can lead to
450 melting. In support of this, biotite and amphibole fragments present in the cataclasite (Fig. 9 &
451 10c) are absent in the vitreous pseudotachylyte (Fig. 7 & 8), suggestive of selective melting of the
452 mineral assemblage due to the lower fracture toughness and melting temperature of these phases
453 (Spray, 2010).

454

455 **5.2. Transient nature of slip zones and slip zone morphology**

456 Despite the deposit only preserving the cumulative history and final state of the debris
457 avalanche, there is evidence to suggest the temporal evolution of the basal shear zones during the
458 flow of the debris avalanche. At Loc. 1, the presence of glassy fragments in the cataclasite

bounding the glass-bearing pseudotachylyte layer (Fig. 7 & 8e-f) suggests that there were at least two melting events. The “glass in layer” and “glass in fragments” have different textures and chemistry (Figs. 8 & 11) so either formed from different mixtures of material in the basal shear zone or under different temperatures, timescales and slip conditions. The original layer became fractured and subsequently a new layer comprising ultracataclasite and pseudotachylyte was formed. This process may have occurred multiple times throughout deposition. The development of a secondary slip layer at this locality was likely a late stage development, potentially induced by the slowing of the lower portion of the flow by loss of momentum and interaction with topography.

Similarly, at Loc. 2, the initially rough topography of the basal contact is cut through by a secondary linear contact (Fig. 3e-f) suggesting gradational shifts in slip rate or overburden to localise slip to different surfaces at different times. Additionally, multiple fractures splay from these surfaces and cross-cut within the shear zone (Fig. 3c-d) suggesting distinct ruptures.

Within the body of the avalanche deposit at Loc. 3, clastic dykes interact with a linear localised shear plane (Fig. 6). The dyke is wider and contains evidence of shear at the contact with the shear plane, indicating it may have terminated at the shear zone during active slip on that contact. In contrast a second clastic dyke at this locality injects through the preserved linear shear plane and is not subjected to any displacement along the shear plane. Therefore, this dyke must have occurred after shearing on this secondary shear plane ceased. This interaction of dykes and shear surfaces is additional evidence supporting the transient nature of active shear surfaces both at the base and within the flow.

### 5.3. Melt chemistry and source rocks

The chemical analyses for the frictional melt glass at Loc. 1 plot between the two bulk rock chemistries of the lower ignimbrite and andesitic upper plate material (Fig. 11). This suggests that a combination of both materials, initially incorporated and sheared in the basal zone, melted to form the glass preserved in the intact basal shear zone.

The more mafic composition of the analysed frictional melt glass fragments within the cataclasite (Fig. 11a), interpreted as remnants of a previous melt-producing shear zone, is likely due to early melting of amphibole and biotite (present in the host rocks and cataclasites). This is also supported by the highly vesicular nature of these fragments, as melting of hydrous phases releases water (e.g. Magloughlin, 2011). Primitive or partial frictional melts are frequently more mafic than more mature melts (Wallace et al., 2019 and references therein) and leave suspended survivor clasts of minerals with higher fracture toughness and/or melting temperature (Spray, 2010). Further melting of the more resistant minerals brings the melt chemistry back towards the bulk chemistry, as seen here with the chemistry of the intact basal pseudotachylyte composition which plots between the andesite and ignimbrite.

### 5.4. Frictional melt rheology evolution

Understanding the development and impact of frictional melting on the debris avalanche requires consideration of its rheology. Here the observations that slip caused frictional melting as well as fragmentation of frictional melt are used to constrain conditions in the debris avalanche during runout. We used the geochemical compositions of the glass (from the preserved layer and the fragment of glass-bearing earlier melt identified within the bounding cataclasite, both from the basal contact at Loc. 1) as input parameters in the GRD viscosity calculator of Giordano et al. (2008) to constrain the temperature (T in Kelvin) dependence of the viscosity ($\eta$ in Pa.s) of the

505 early frictional melt present in fragments ($\eta_e$) and late frictional melt forming the main basal
506 pseudotachylyte ($\eta_l$):

507 $$log\eta_e = A + \frac{B}{T(K) - C} \quad (1)$$

508 Table 1 provides the values of A, B and C (where B and C are adjustable parameters controlled
509 by composition and A is a constant independent of composition related to the viscosity at infinite
510 temperature, see Giordano et al. (2008)) to model both melts (Fig 12a). The chemical compositions
511 vary significantly locally due to the presence of small unhomogenised melt filaments (schlieren),
512 which would have contrasting rheologies. However, the chemical compositions input do not
513 include the water concentrations which would have likely been transiently present in the frictional
514 melts owing to the presence of amphibole in the host rock (e.g. Wallace et al., 2019). Here, we
515 assume the melt phase contained a nominal 0.1 wt.% water concentration in this low-pressure
516 environment.

517 (Insert Table. 1 here)

518 The frictional melts described here contain variable fractions of suspended crystals and
519 bubbles, known to impact the rheology and contribute to a non-Newtonian behaviour (Caricchi et
520 al., 2007; Lavallée et al., 2007; Truby et al., 2015; Coats et al., 2018). Here we consider the
521 influence of crystals (i.e., fraction, shape and maximum packing) using the two-phase rheology
522 calculator from Costa et al. (2009). We first constrained the solid fraction present in the
523 pseudotachylyte (i.e., surviving crystals and lithics) via SEM image analysis using the ImageJ
524 online toolbox (Schneider et al., 2012). We estimated the solid fraction in the early
525 pseudotachylyte at 0.25 and late pseudotachylyte at 0.43 and the aspect ratio of the particles as
526 1.761 in the early and 1.684 in the late pseudotachylyte. Then, following guidelines from Mueller
527 et al. (2010), we used the aspect ratio of the solid fraction to define a critical maximum packing
528 of a monodisperse distribution $\varphi_{m,m}$ for both suspensions at 0.57. However, due to the

polydispersivity ($\delta$) of the solid fraction, the true maximum packing is higher. We used Phan et al. (1998) to define the polydispersivity where $\delta = \frac{r_{sd}}{\langle r \rangle}$ where $r_{sd}$ is the standard deviation of the fragment radii (3.00 and 2.71 for the fragment and layer respectively) and $\langle r \rangle$ is the mean of the fragment radii (3.66 and 3.67 for the fragment and layer respectively). This is based on measurements from 205 particles from the glass bearing fragment and 417 particles in the preserved layer over an analysis area of 200 and 100 μm$^2$ respectively (see supplementary data). Subsequently, the polydispersivity of the fragment $(\delta_e)$ and later preserved layer $(\delta_l)$ pseudotachylytes were input into the fitting equation from Klein et al. (2017) substituting the monodisperse maximum packing of spheres $(\varphi_{m,0})$ for our previously defined monodisperse packing of the solid fraction's aspect ratio $(\varphi_{m,m} = 0.57)$. This defines the true maximum packing of the solid fraction of the early fragment $(\varphi_{m,e})$ and late preserved layer $(\varphi_{m,l})$ such that:

$$\varphi_{m,e} = (1 - \varphi_{m,m}) e^{(-\delta_e * \varphi_{m,m})} \quad (2)$$

These geometrical parameters were then used in the Costa et al. (2009) model to define the apparent viscosity of the frictional melt suspensions; here, considering the mass movements' runout speeds of >10 ms$^{-1}$ (Legros, 2002 and references therein) and the preserved frictional melt thickness of 12 mm, we estimated the maximum frictional melt strain rate at $10^3$ s$^{-1}$ for use in our calculations (Fig.12b; Table 1). [Whilst we posit that melt generation and thus melt thickness varied temporally and spatially, we used the preserved frictional melt layer thickness to define strain rate here to illustrate the impact of particles on suspension viscosity.] We observe that the presence of solid particles in the frictional melt significantly increase the range of probable viscosities which impact slip during the debris avalanche. Yet, further constraints of suspension viscosity are difficult without knowledge of temperature conditions in the melt.

551 Frictional melting has commonly been described to be a disequilibrium process occurring
552 via selective melting of mineral phases (Spray, 1992, 2010; Shimamoto and Lin, 1994; Lin and
553 Shimamoto, 1998; Wallace et al., 2019). This provides a framework to evaluate frictional melt
554 temperature based on mineral breakdown temperature. Considering that the frictional melting
555 likely involved both wall rocks and that the pyroxenes, some plagioclase and few amphiboles
556 survived implies that most of the amphiboles, any biotite inherited from the ignimbrite, the
557 andesitic interstitial glass and some of the plagioclase likely underwent melting. This analysis
558 suggests that the frictional melt may have reached temperatures of approximately 1200-1300°C.
559 At such temperatures, the viscosity of the frictional melt preserved in the basal layer would have
560 been $10^{5.1}$ -$10^{4.3}$ Pa.s (for the highest silica melt chemistry) and the apparent viscosity of the
561 suspensions at a strain rate of $10^3$ $s^{-1}$ ($\eta_{app}$) approximately $10^{5.8}$ – $10^{5.1}$ Pa.s (assuming a nominal
562 0.1 wt.% water dissolved in the melt).

563 The theory of heat conduction detailed by Carslaw and Jaeger (1959) can be used to
564 estimate slip conditions required to generate temperature change ($\Delta T$) :

565 $$\Delta T = \frac{\mu \sigma_n V \sqrt{t}}{\rho C_p \sqrt{\pi k}} \quad (3)$$

566 Considering a friction coefficient ($\mu$) of 0.85 (at static conditions) (Byerlee, 1978), a normal stress
567 ($\sigma_n$) of 2.6 MPa [based on an overburden of 100 m and a bulk rock density ($\rho$) of 2656.6 $kg.m^{-3}$
568 (as determined by He-pycnometry)], a specific heat capacity ($C_p$) of 900 $J.kg^{-1}.K^{-1}$, and a thermal
569 diffusivity ($k$) of $10^{-6}$ $m^2.s^{-1}$, we can bracket slip velocity ($V$) and duration ($t$) along the basal
570 contact. Given that distance ($d$) is proportional to the products of slip rate and duration, $d= Vt$, the
571 above analysis suggests that frictional melting (reaching a nominal temperature of 1250ºC), would
572 have occurred in <2 m if the slip velocity was greater than 5 $m.s^{-1}$. Figure 12c shows that for more
573 rapid slip rates, the distance of slip required would have needed to be shorter. This does not agree
574 with the observation that only a thin pseudotachylyte was observed at much greater runout

575 distances of 24 km. Yet, considering that the basal contact did not generate (or preserve) a
576 pseudotachylyte at a slip distance of 17.5 km, it suggests that the slip conditions must have locally
577 evolved rapidly during the avalanche, highlighting the transient nature of slip during debris
578 avalanches, including the potential reduction of $\mu$ during dynamic slip. Thus, we must turn to other
579 proxies to define local slip rate conditions that led to frictional melting.

580 (Insert Fig. 12 here)

581 The early occurrence of frictional melt fragmentation, as witnessed by the presence of
582 pseudotachylyte fragments (with different chemistry to the main pseudotachylyte) in the marginal
583 cataclastic region of the shear zone, demands further appraisal. Silicate melts are viscoelastic
584 bodies which abide by Maxwell's structural relaxation concept (Dingwell and Webb, 1989), where
585 the timescale of relaxation ($\tau$) is proportional to the ratio between the melt's shear viscosity ($\eta$)
586 and the elastic modulus at infinite frequency ($G_\infty$, approximated at $10^{10}$ Pa for silicate melts at
587 relevant conditions; Webb and Dingwell, 1990):

588 $$\tau = \frac{\eta}{G_\infty} \quad (4)$$

589 In rheological analysis, if the timescale of observation ($t_{obs}$) approaches the relaxation timescale,
590 the material exhibits increasingly elastic behaviour and may rupture if the accumulated stress is
591 sufficient. This can be accessed via the dimensionless Deborah number ($De$), whereby $De_0 = \frac{\tau}{t_{obs}}$.
592 It has been found that silicate melts tend to rupture at strain rates two orders of magnitude lower
593 than that predicted by viscoelasticity theory; that is, at a critical Deborah limit, $De_{c,0} = 10^{-2}$
594 (Webb and Dingwell, 1990). Thus, the critical timescale for rupture has commonly been simplified
595 to $\tau_c = \frac{\eta}{De_{c,0} G_\infty}$ (Lavallée et al., 2015). Given that the inverse of the relaxation timescale
596 corresponds to the structural relaxation timescale, $\dot{\varepsilon} = 1/\tau$, Lavallée et al. (2015) coined the

following expression to define the strain rate at which a frictional melt would undergo rupture ( $\dot{\varepsilon}_{max}$):

$$\dot{\varepsilon}_{max} = \frac{De_{c,0} G_{\infty}}{\eta} \quad (5)$$

Assuming that shear is distributed across the entire thickness of the frictional melt layer ($z \cong$ 12 mm), they suggest that we can estimate the maximum slip rate ($V_{max}$) using

$$V_{max} = \frac{De_{c,0} G_{\infty} z}{\eta} \quad (6)$$

Considering an early frictional melt viscosity ($\eta_e$) estimate of $10^{4.4}$ Pa.s, Eq. 5 would suggest that the melt phase underwent a strain rate greater than $10^{3.6}$ $s^{-1}$ and Eq. 6 would constrain the local slip velocity at 46.9 $m.s^{-1}$. However, the presence of the solid fragments and bubbles in the melt layer would have also modified the rheological conditions leading to rupture (e.g. Coats et al., 2018); thus any modelling of frictional melt rheology should account for the complexity borne by suspended particles. Here we detail how to implement this analysis. Cordonnier et al. (2012) suggested that the fraction of crystals in suspension ($\varphi_x$) would lower the critical Deborah number $De_{c,x}$ following:

$$De_{c,x} = De_{c,0}\left(1 - \frac{\varphi_x}{\varphi_{m,e}}\right) \quad (7)$$

where $\varphi_{m,e}$ is the maximum packing value estimated for the frictional melt at 0.73 for the early fragmented pseudotachylyte and 0.71 for the later preserved layer. The fraction of bubbles $\varphi_b$ in the suspension would have similarly lowered the critical Deborah limit of the suspension ($De_{c,s}$), which according to Coats et al. (2019) would follow:

$$De_{c,s} = 1.7 \times 10^{-4} \varphi_b + De_{c,x} \quad (8)$$

which can be rewritten as

$$De_{c,s} = 1.7 \times 10^{-4}\varphi_b + De_{c,0}\left(1 - \frac{\varphi_x}{\varphi_{m,e}}\right) \quad (9)$$

So, considering this failure criterion in our previous analysis of maximum strain rate and slip velocity experienced by the frictional melt, we can rewrite Eq. 5 and 6, by considering $De_{c,s}$ instead of $De_{c,0}$, obtaining:

$$\dot{\varepsilon}_{max} = \left(1.7 \times 10^{-4}\varphi_b + 10^{-2}\left(1 - \frac{\varphi_x}{\varphi_{m,e}}\right)\right)\frac{G_\infty}{\eta} \quad (10)$$

And

$$V_{max} = \left(1.7 \times 10^{-4}\varphi_b + 10^{-2}\left(1 - \frac{\varphi_x}{\varphi_{m,e}}\right)\right)\frac{G_\infty z}{\eta} \quad (11)$$

respectively. As the fragmented pseudotachylyte has interstitial melt with a viscosity of $10^{4.4}$ Pa.s and contains $\varphi_x = 0.25$ and $\varphi_b = 0.14$, we estimate rupture occurred when the strain rate exceeded ~$10^{3.4}$ $s^{-1}$ which would have occurred when the slip velocity exceeded at least 31 $m.s^{-1}$ during debris avalanche (Fig 12d); this critical slip velocity (for fragmentation) may have been higher for less evolved schlieren present in this early frictional melt. The same calculation for the later formed preserved layer using interstitial melt viscosity $(\eta_l)$ of $10^{4.7}$ Pa.s, $\varphi_x = 0.43$, $\varphi_b = 0.15$ and $\varphi_{m,l} = 0.71$ gives a lower maximum velocity of 9.6 $m.s^{-1}$ for the most evolved schlieren within the late frictional melt (but higher values for the less evolved melt filaments). So, these rheological constraints provide a view that the slip velocity varied during the debris avalanche.

Finally, in order to assess the rheological impact of frictional melt on debris avalanches, we compare the shear resistance ($\sigma_s$) of the modelled melt layers to the shear resistance that would occur in a purely frictional, rock-rock slip environment (i.e., without melt). To do this, we use the viscosity equation:

639 $$\sigma_s = \eta_{app}\dot{\varepsilon} \quad (12)$$

640 where the strain rate for the layer modelled is calculated by:

641 $$\dot{\varepsilon} = \frac{V}{z} \quad (13)$$

642 Frictional melt suspension viscosity ($\eta_{app}$) previously calculated (see Table 1) following Costa et
643 al. (2009) constrain the range of shear resistance imposed by the frictional melt onto slip at 4.7-
644 56.1 MPa, evolving to 22.1-260.4 MPa with further slip (under the same conditions). In contrast,
645 the frictional resistance of rock-rock slip at the base of the deposit may be estimated using
646 Byerlee's frictional law of $\sigma_s = \mu\sigma_n$ (Byerlee, 1978); assuming a friction coefficient of 0.85 and
647 a normal stress, $\sigma_n = \rho g D = 2.6$ MPa, we estimate the shear resistance during rock-rock sliding
648 at 2.2 MPa. Comparing the shear resistances offered by rock-rock friction versus frictional melt,
649 we find that the shear resistance calculated for the melt layer at $10^3$ $s^{-1}$ strain rate exceeds that
650 predicted by Byerlee's frictional law. Yet, we surmise that the rate weakening tendency of rock-
651 rock friction (Fialko and Khazan, 2005) would likely promote even lower shear resistances at the
652 slip rates of meters/seconds described in this section. However, local variations in chemistry, solid
653 fraction and temperature would have promoted strain localisation which may have drastically
654 impacted the resultant shear resistance during slip. It must be noted here, that the modelled
655 apparent viscosities of the frictional melts may have been overestimated as they are constrained at
656 a strain rate ($10^3$ $s^{-1}$) exceeding the empirically validated strain rate limit ($10^{-1}$ $s^{-1}$) of the Costa et
657 al. (2009) model. Beyond that limit, the model assumes (hence predicts) that the apparent viscosity
658 no longer decreases as a function of strain rate (i.e., that slip with frictional melt no longer
659 undergoes rate weakening at such extreme rates); thus the shear resistance (calculated for a given
660 viscosity) increases with strain rate, though this remains untested. Further rheological experiments
661 at such extreme rates are required to improve our ability to model the rapid shear regime extant in
662 sector collapse events.

663 ## 6. Discussion

664 ### 6.1. Emplacement style

665 The palaeotopography of the original land surface included ridges and gullies as evidenced
666 by the preserved palaeotopography and lahar deposits which are restricted to narrow channels in
667 the ignimbrite. Clastic dyking may have resulted from the avalanche crossing fluid rich areas of
668 palaeotopography such as riverbeds, or simply saturated regions of the porous ignimbrite. Local
669 flow directions at Loc. 1 (Fig. 2) indicate that the debris avalanche was at least partially directed
670 by local topography, which may be especially relevant near the thinned margins.

671 In each locality investigated there appears to be very little range in lithic composition.
672 Although little literature exists on the composition of eruptive and intrusive products from Pichu
673 Pichu, the observations made here suggest that the volcanic edifice-forming rocks are consistent
674 with intermediate volcanic products typical of a compound volcano present in the Andes. The
675 homogeneity of the surviving clasts within the flow in the areas studied therefore suggests there
676 was limited internal shear that would have enhanced mixing of different lithologies during the
677 debris avalanche. This is supported by the sharp contact between compositionally different flow
678 packages at Loc. 1 (see Fig. 2e-f). Such separation of flow packages suggests that overall, the flow
679 mostly moved as discrete bodies, though without knowledge of the volcanic units incorporated
680 this interpretation is speculative. Higher up in the flow at Loc. 3 away from high shear at the basal
681 contact, large clasts have been transported intact. In this survey, as all the studied shear structures
682 were all in distal localities, it is difficult to convey any constraint about coherence within the core
683 of the flow. Several field mapping studies of collapse deposits have previously noted that mixed-
684 matrix supported facies were rare in the deposit core, but were more common in marginal regions
685 (Glicken, 1998; Belousov et al., 1999). These studies have highlighted that the centre of deposits
686 and proximal areas consist of larger blocks in block-supported facies.

687

688 **6.2. Evolving degree of strain localisation**

689 The basal sliding surface or shear zone of a mass movement is subjected to extreme shear
690 conditions (Erismann and Abele, 2001). As noted at Loc. 1 there is evidence for intense shearing
691 in the lower 2-3 m of the flow, causing the destruction of large clasts, forming a matrix-dominated,
692 well-sorted granular layer. The presence of a matrix-supported basal layer has previously been
693 observed at other avalanche deposits worldwide, such as at Parinacota (Chile) where structureless
694 sedimentary layers occur at the base of each deposit and are interpreted to originate from the
695 localisation of shear during emplacement (Clavero et al., 2002). Similarly, the small grain sizes in
696 the lower 1 m at the base of multiple debris avalanche deposits from Shiveluch (Kamchatka
697 peninsula, Russia), has also been interpreted as the result of shear localisation at the base of a
698 debris flow (Belousov et al., 1999). Although none are associated with a basal pseudotachylyte, it
699 is an indicator for the common occurrence of basal shear localisation and comminution in volcanic
700 debris avalanches. The extreme localisation to produce frictional melting, as seen at Loc. 1 in this
701 study, is still rarely reported. However, earlier studies on this phenomenon at field sites such as
702 Langtang (Nepal: Masch et al., 1985) and Kofels (Austria; Erismann, 1979) have been joined by
703 more recent studies on Markagunt gravity slide in Utah (Hacker et al., 2014), Heart Mountain in
704 Wyoming (Goren et al., 2010), Mont Dore volcanic massif (France; Bernard and van Wyk de
705 Vries, 2017) and a rockslide near Kanchenjunga (Nepal; Weidinger and Korup, 2009) where
706 further landslide generated pseudotachylytes have been identified.

707 Observations made in Loc. 2 suggest that basal granular zones may be subjected to a high
708 degree of strain localisation, as observed by an area of pervasive cataclastic shear crosscut by a
709 fault surface, showing slip transfer upon enhanced localisation. Such cross-cutting behaviour,
710 indicative of an increased degree of strain localisation, was further observed in the intra-body

711 shear zones, suggesting that these switches in the degree of strain localisation may not necessarily
712 be restricted to the basal shear zone, but may affect the development of the avalanche as a whole.
713 This may be likely if shear occurs in an unfavourable region as in cases where a contact is uneven
714 with asperities (see Loc. 2) or if local topography slopes against the deposit flow direction or
715 during acceleration or deceleration phases. Rough surface topology across all scales would locally
716 induce higher normal stresses which would respectively promote higher shear stresses (and
717 intergranular forces) in this region of the flow, as illustrated by a sketch diagram in Figure 13.
718 This concentration of stress at the asperities may have promoted the rupture in the granular
719 medium of a new, smoother surface and facilitate flow with lower frictional resistance. This would
720 either act to shift shear to above the asperity (Fig. 13c) and/or remove some or all of the basal
721 asperity (Fig. 13d), incorporating the fragmented materials in the flow, and promoting shear on a
722 smooth surface as seen at Loc. 2 (Fig. 3e-f). Evidence for both mechanisms are seen, first by the
723 generation of secondary slip surfaces and second by incorporation of ignimbrite material into the
724 flow deposit. The Koefels landslide in Austria underwent a similar process but at a larger scale,
725 forming new internal slip surfaces upon encountering a topographic barrier (in this case a valley
726 wall) (Erismann, 1979). This is somewhat similar to the decoupling process in pyroclastic density
727 currents and block-and-ash flows, where the dilute upper portion of the flow can detach from the
728 lower flow and override a topographic barrier and even travel in a different direction to the lower
729 flow (Fisher, 1995; Douillet et al., 2013). Here, the outcrops at Loc. 1 show 2 distinct zones of
730 shear localisation at different levels within the flow body, similar to the suggestion of De Blasio
731 and Elverhøi (2008).

732 (Insert Fig. 13 here)

733

734 **6.3. Frictional melting**

735 As pseudotachylytes were not ubiquitous along the basal contact, we advance that the
736 generation of frictional melt at the base of debris avalanches may be considered to be both spatially
737 and temporally discontinuous. The occurrence of a fluidised basal layer with enhanced injection
738 and mixing, seen at Loc. 3 and in other landslides (Anders et al., 2010; Craddock et al., 2012) can
739 prevent the strain localisation necessary for frictional melting. Melt formation in volcanic
740 collapses is highly dependent on the conditions (including normal stress from overburden and pore
741 pressure) (Legros, 2002; Nielsen et al., 2008; Violay et al., 2014), extent and rate of shear
742 localisation (Magloughlin and Spray, 1992; De Blasio and Elverhøi, 2008), heat generation versus
743 diffusion away from slip surface (Carslaw and Jaeger, 1959), any residual heat from volcanism,
744 surface topography and roughness (Nielsen et al., 2010), and the melting points and shear strength
745 of the materials (Spray, 1992), many of which would vary and evolve during transport. This may
746 in part explain the common absence of pseudotachylyte at the basal contacts of debris avalanche
747 deposits worldwide, which may also be a result of alteration or destruction (Kirkpatrick and Rowe,
748 2013). As modelled in section 5.4, debris avalanches flowing at high rates (along one or several
749 thin shear zones) may promote shear rates likely to exceed the structural relaxation of frictional
750 melts to induce brittle failure, preventing preservation.

751 The maximum strain rates that may be accommodated by the thickness of the
752 inhomogeneous melt layer observed indicates that the flow exceeded ~31 $m.s^{-1}$ to fragment it.
753 However, the higher modelled viscosity of the preserved layer suggests that it would have
754 fragmented at slip velocities exceeding 9.6 $m.s^{-1}$ (at the estimated temperatures). As the layer has
755 remained intact, this suggests that the flow slowed between the fragmentation of the early melt-
756 bearing layer and the formation of the preserved melt-bearing layer. This may also imply that the
757 shear was localised elsewhere, a hypothesis supported by the occurrence of a secondary slip
758 surface above the basal contact at this locality, or the layer preserved in the outcrop was a late
759 stage feature formed as the flow slowed. Thus, slip velocity may dynamically vary during

760 transport, as a function of distance, palaeotopography and strain partitioning onto different fault
761 surfaces; such contrasting slip conditions may promote compressional and extensional regimes in
762 the flow, which could induce secondary shear zones and intrusion of clastic dykes.

763 Although frictional melts are commonly regarded as potential lubricating layers promoting
764 increased runout distances (Erismann, 1979; De Blasio and Elverhøi, 2008), the rheological
765 comparison of the apparent viscosity to Byerlee (1978) friction indicates that frictional melting is
766 unlikely to have lessened the basal shear resistance at the high shear rates expected; even though
767 the early frictional melt (prior to fragmentation) exhibited a relatively low apparent viscosity.
768 Additionally, variation in melt layer thickness, temperature, and the incorporation of both exsolved
769 and dissolved water from the breakdown of amphiboles could have rheologically impacted the
770 development of frictional melts and promoted lubrication through time. If the formation of
771 pseudotachylyte is a cyclic process in which melting may be followed by fragmentation (if strain
772 rate is too high) and slip re-localisation onto a new fault plane, then the lubricating or viscous
773 braking effects of frictional melts may equally be cyclic. It must be noted that variability in
774 chemistry and, importantly, crystallinity during selective melting and melt homogenisation
775 controls the rheological evolution of frictional melt (Spray, 2010; Wallace et al., 2019) and
776 whether lubrication or viscous brake locally develops with slip.

777

778 **7. Concluding remarks**

779 The Arequipa volcanic landslide deposit originated from the sector collapse of Pichu Pichu
780 volcano and forms an area of elevated hummocky topography approximately 300 m thick at its
781 maxima, which extends 26 km west from the dissected volcanic complex in a broad, fan-like shape
782 that covers >100 $km^2$. The andesitic debris avalanche, which likely exceeded 20 $km^3$ in volume,
783 ramped up over a palaeotopography of ignimbrite during runout.

784 The subsequent deposition of eruption products of other proximal volcanoes and the
785 incision of rivers into the deposit obscures the original topography. However, river valleys reveal
786 the basal contact and structures within the lower portion of the flow. Field examination, chemical
787 analyses and microstructural observations highlight the complex nature of shear during the debris
788 avalanche. We observed evidence of a variety of shear deformation mechanisms (cataclasis and
789 frictional melting), degrees of strain localisation, and strain partitioning across the body of the
790 flow (summarised in Fig. 14).

791 (Insert Fig. 14 here)

792 The basal contacts show varying degrees of shear localisation. The first example evidences
793 a high level of shear with near total fragmentation of clasts near the basal contact and extreme
794 localisation of shear to form a thin layer of pseudotachylyte. Fragments of pseudotachylyte within
795 the cataclasite at the base suggests multiple generations of melt. Geochemical results combined
796 with rheology modelling are used to suggest that the fragmentation of melt layers could be
797 attributed to high strain rates that forced the melt into brittle rupture, thus limiting the chance of a
798 persisting melt layer. Contrastingly, the second locality studied has a more diffuse basal shear
799 zone, less fragmentation of clasts, multiple fracture sets and crosscutting slip surfaces that show
800 slip zone evolution and indicate more distributed shear.

801 Within the lower portion of the debris avalanche body, at several localities, secondary
802 shear zones are observed in the deposit. This highlights the propensity to delocalise shear from the
803 basal plane to be accommodated on other discrete planes. Additionally, we note the presence of
804 clastic dyking which likely originates from the basal plane and suggests the presence of a
805 pressurised, fluidised layer in some areas that may have been enhanced by crossing of river beds
806 or water saturation of the underlying porous ignimbrite. The interaction of clastic dykes, shear

807 planes and the juxtaposition of distinct flow units suggests that active shearing planes acted as
808 barrier layers limiting material mixing and causing segregation of the flow.

809 We conclude that shear localisation can occur at both the basal contact and on discrete
810 planes within the flow and that frictional melting at the debris flow base may be possible at areas
811 of extreme localisation of shear. However, it is unlikely that frictional melt aided lubrication at
812 the base or that it persisted throughout the debris avalanche deposition, instead local deformation
813 mechanisms at the flow base likely switched rapidly. The localisation of shear can therefore
814 change both through time and spatially across the flow due to topographic, lithological and
815 environmental changes of the land surface.

## 8. Acknowledgements

This work was conducted during a PhD study supported by the Natural Environment Research Council (NERC) EAO Doctoral Training Partnership and is fully funded by NERC whose support is gratefully acknowledged (Grant Number NE/L002469/1). We acknowledge financial support from the European Research Council Starting Grant on Strain Localisation in Magma (SLiM, No. 306488) and Jackie Kendrick was supported by an Early Career Fellowship of the Leverhulme Trust (ECF-2016-325). We also thank Tom Knott (University of Leicester) for XRF measurements and Jonathan Fellowes (University of Manchester) for technical assistance during EPMA analysis. We thank the editor Joao Hippertt and an anonymous reviewer for their well-thought, precise and constructive comments.

## 9. References

Acocella, V., Puglisi, G., 2010. Hazard Mitigation of Unstable Volcanic Edifices. EOS Transactions 91. https://doi.org/10.1029/2010EO400002

Aguilar Contreras, R., Thouret, J.-C., Samaniego Eguiguren, P., 2016. Actividad eruptiva en sistemas de larga duración: relaciones entre el complejo post-caldérico Chachani y las ignimbritas Plio-cuaternarias de la cuenca de Arequipa (Perú). Instituto Geológico, Minero y Metalúrgico – INGEMMET.

Anders, M., Fouke, B., Zerkle, A., Tavarnelli, E., Alvarez, W., Harlow, G., 2010. The Role of Calcining and Basal Fluidization in the Long Runout of Carbonate Slides: An Example from the Heart Mountain Slide Block, Wyoming and Montana, U.S.A. Journal of Geology 118. https://doi.org/10.1086/656383

Arabnia, O., Sklar, L., 2016. Experimental Study of Particle Size Reduction in Geophysical Granular Flows. International Journal of Erosion Control Engineering 9, 122–129.

https://doi.org/10.13101/ijece.9.122

Belousov, A., Belousova, M., Voight, B., 1999. Multiple edifice failures, debris avalanches and associated eruptions in the Holocene history of Shiveluch volcano, Kamchatka, Russia. Bulletin of Volcanology 61, 324–342. https://doi.org/10.1007/s004450050300

Benson, P., Heap, M.J., Lavallée, Y., Flaws, A., Hess, K.-U., Selvadurai, P., Dingwell, D., Schillinger, B., 2012. Laboratory simulations of tensile fracture development in a volcanic conduit via cyclic magma pressurisation. Earth and Planetary Science Letters s 349–350, 231–239. https://doi.org/10.1016/j.epsl.2012.07.003

Bernard, K., van Wyk de Vries, B., 2017. Volcanic avalanche fault zone with pseudotachylite and gouge in French Massif Central. Journal of Volcanology and Geothermal Research 347, 112–135. https://doi.org/10.1016/J.JVOLGEORES.2017.09.006

Biek, R.F., Rowley, P.D., Hacker, D.B., 2019. The Gigantic Markagunt and Sevier Gravity Slides Resulting from Mid-Cenozoic Catastrophic Mega-Scale Failure of the Marysvale Volcanic Field, Utah, USA. https://doi.org/10.1130/FLD056

Brodsky, E.E., Kanamori, H., 2001. Elastohydrodynamic lubrication of faults. Journal of Geophysical Research: Solid Earth 106, 16357–16374. https://doi.org/10.1029/2001JB000430

Byerlee, J., 1978. Friction of Rocks. Pure and Applied Geophysics 116, 615–626. https://doi.org/10.1007/bf00876528

Calder, E.S., Luckett, R., Sparks, R.S.J., Voight, B., 2002. Mechanisms of lava dome instability and generation of rockfalls and pyroclastic flows at Soufrière Hills Volcano, Montserrat. Geological Society, London, Memoirs 21, 173–190. https://doi.org/10.1144/GSL.MEM.2002.021.01.08

863 Campbell, C.S., Cleary, P.W., Hopkins, M., 1995. Large-scale landslide simulations: Global
864 deformation, velocities and basal friction. Journal of Geophysical Research: Solid Earth
865 100, 8267–8283. https://doi.org/10.1029/94JB00937

866 Caricchi, L., Burlini, L., Ulmer, P., Gerya, T., Vassalli, M., Papale, P., 2007. Non-Newtonian
867 rheology of crystal-bearing magmas and implications for magma ascent dynamics. Earth
868 and Planetary Science Letters 264, 402–419. https://doi.org/10.1016/j.epsl.2007.09.032

869 Carslaw, H.S., Jaeger, J.C., 1959. Conduction of heat in solids. Clarendon Press, Oxford.

870 Cecchi, E., van Wyk de Vries, B., Lavest, J.-M., 2004. Flank spreading and collapse of weak-
871 cored volcanoes. Bulletin of Volcanology 67, 72–91. https://doi.org/10.1007/s00445-004-
872 0369-3

873 Clavero, J., Sparks, R.S.J., Huppert, H., WB, D., 2002. Geological constraints on the
874 emplacement mechanism of the Parinacota debris avalanche, Northern Chile. Bulletin of
875 Volcanology 64, 40–54. https://doi.org/10.1007/s00445-001-0183-0

876 Coats, R., Kendrick, J., Wallace, P., Miwa, T., Hornby, A., Ashworth, J., Matsushima, T.,
877 Lavallée, Y., 2018. Failure criteria for porous dome rocks and lavas: A study of Mt. Unzen,
878 Japan. Solid Earth 9, 1299–1328. https://doi.org/10.5194/se-9-1299-2018

879 Cordonnier, B., Caricchi, L., Pistone, M., Castro, J., Hess, K.-U., Gottschaller, S., Manga, M.,
880 Dingwell, D.B., Burlini, L., 2012. The viscous-brittle transition of crystal-bearing silicic
881 melt: Direct observation of magma rupture and healing. Geology 40, 611–614.
882 https://doi.org/10.1130/G3914.1

883 Costa, A., Caricchi, L., Bagdassarov, N., 2009. A model for the rheology of particle-bearing
884 suspensions and partially molten rocks. Geochemistry, Geophysics, Geosystems 10.
885 https://doi.org/10.1029/2008GC002138

886 Craddock, J.P., Geary, J., Malone, D.H., 2012. Vertical injectites of detachment carbonate
887 ultracataclasite at White Mountain, Heart Mountain detachment, Wyoming. Geology 40,
888 463–466. https://doi.org/10.1130/G32734.1

889 Davies, T.R., McSaveney, M.J., 2009. The role of rock fragmentation in the motion of large
890 landslides. Engineering Geology 109, 67–79.
891 https://doi.org/https://doi.org/10.1016/j.enggeo.2008.11.004

892 Davies, T.R.H., 1982. Spreading of rock avalanche debris by mechanical fluidization. Rock
893 Mechanics 15, 9–24. https://doi.org/10.1007/BF01239474

894 Day, S.J., 1996. Hydrothermal pore fluid pressure and the stability of porous, permeable
895 volcanoes. Geological Society, London, Special Publications 110, 77–93.
896 https://doi.org/10.1144/gsl.sp.1996.110.01.06

897 De Blasio, F.V., 2011. Landslides in Valles Marineris (Mars): A possible role of basal
898 lubrication by sub-surface ice. Planetary and Space Science 59, 1384–1392.
899 https://doi.org/10.1016/J.PSS.2011.04.015

900 De Blasio, F.V., Elverhøi, A., 2008. A model for frictional melt production beneath large rock
901 avalanches. Journal of Geophysical Research: Earth Surface 113, n/a-n/a.
902 https://doi.org/10.1029/2007JF000867

903 de Silva, S.L., Francis, P.W., 1990. Potentially active volcanoes of Peru-Observations using
904 Landsat Thematic Mapper and Space Shuttle imagery. Bulletin of Volcanology 52, 286–
905 301. https://doi.org/10.1007/BF00304100

906 Di Toro, G., Hirose, T., Nielsen, S., Pennacchioni, G., Shimamoto, T., 2006. Natural and
907 experimental evidence of melt lubrication of faults during earthquakes. Science 311, 647–
908 649. https://doi.org/10.1126/science.1121012

Dingwell, D.B., Webb, S.L., 1989. Structural relaxation in silicate melts and non-Newtonian melt rheology in geologic processes. Physics and Chemistry of Minerals 16, 508–516. https://doi.org/10.1007/bf00197020

Douillet, G.A., Tsang-Hin-Sun, È., Kueppers, U., Letort, J., Pacheco, D.A., Goldstein, F., Von Aulock, F., Lavallée, Y., Hanson, J.B., Bustillos, J., Robin, C., Ramón, P., Hall, M., Dingwell, D.B., 2013. Sedimentology and geomorphology of the deposits from the August 2006 pyroclastic density currents at Tungurahua volcano, Ecuador. Bulletin of Volcanology 75, 765. https://doi.org/10.1007/s00445-013-0765-7

Erismann, T., Abele, G., 2001. Dynamics of Rockslides and Rockfalls. https://doi.org/10.1007/978-3-662-04639-5

Erismann, T.H., 1979. Mechanisms of large landslides. Rock Mechanics 12, 15–46. https://doi.org/10.1007/bf01241087

Ferri, F., Di Toro, G., Hirose, T., Han, R., Noda, H., Shimamoto, T., Quaresimin, M., de Rossi, N., 2011. Low- to high-velocity frictional properties of the clay-rich gouges from the slipping zone of the 1963 Vaiont slide, northern Italy. Journal of Geophysical Research: Solid Earth 116. https://doi.org/10.1029/2011JB008338

Fialko, Y., Khazan, Y., 2005. Fusion by earthquake fault friction: Stick or slip? Journal of Geophysical Research 110. https://doi.org/10.1029/2005JB003869

Fisher, R. V., 1995. Decoupling of pyroclastic currents: hazards assessments. Journal of Volcanology and Geothermal Research 66, 257–263. https://doi.org/10.1016/0377-0273(94)00075-R

Giordano, D., Russell, J.K., Dingwell, D.B., 2008. Viscosity of magmatic liquids: A model. Earth and Planetary Science Letters 271, 123–134.

https://doi.org/10.1016/J.EPSL.2008.03.038

Glicken, H., 1998. Rockslide-debris avalanche of May 18, 1980, Mount St. Helens Volcano, Washington. Bulletin of the Geological Survey of Japan 49, 96–677.

Glicken, H., 1991. Sedimentary Architecture of Large Volcanic-Debris Avalanches., Sedimentation in Volcanic Settings. https://doi.org/10.2110/pec.91.45.0099

Goren, L., Aharonov, E., Anders, M.H., 2010. The long runout of the Heart Mountain landslide: Heating, pressurization, and carbonate decomposition. Journal of Geophysical Research: Solid Earth 115. https://doi.org/10.1029/2009JB007113

Hacker, D.B., Biek, R.F., Rowley, P.D., 2014. Catastrophic emplacement of the gigantic Markagunt gravity slide, southwest Utah (USA): Implications for hazards associated with sector collapse of volcanic fields. Geology 42, 943–946. https://doi.org/10.1130/G35896.1

Heap, M.J., Faulkner, D.R., Meredith, P.G., Vinciguerra, S., 2010. Elastic moduli evolution and accompanying stress changes with increasing crack damage: implications for stress changes around fault zones and volcanoes during deformation. Geophysical Journal International 183, 225–236. https://doi.org/10.1111/j.1365-246X.2010.04726.x

Hunt, J.E., Cassidy, M., Talling, P.J., 2018. Multi-stage volcanic island flank collapses with coeval explosive caldera-forming eruptions. Scientific Reports 8, 1146. https://doi.org/10.1038/s41598-018-19285-2

Iverson, R.M., George, D.L., Allstadt, K., Reid, M.E., Collins, B.D., Vallance, J.W., Schilling, S.P., Godt, J.W., Cannon, C.M., Magirl, C.S., Baum, R.L., Coe, J.A., Schulz, W.H., Bower, J.B., 2015. Landslide mobility and hazards: implications of the 2014 Oso disaster. Earth and Planetary Science Letters 412, 197–208. https://doi.org/10.1016/J.EPSL.2014.12.020

Johnson, B.C., Campbell, C.S., Melosh, H.J., 2016. The reduction of friction in long runout

landslides as an emergent phenomenon. Journal of Geophysical Research: Earth Surface 121, 881–889. https://doi.org/10.1002/2015JF003751

Kaneoka, I., Guevara, C., 1984. K-Ar determinations of late Tertiary and Quaternary Andean volcanic rocks, Southern Peru. GEOCHEMICAL JOURNAL 18, 233–239. https://doi.org/10.2343/geochemj.18.233

Kawamura, S., Miura, S., 2013. Rainfall-induced failures of volcanic slopes subjected to freezing and thawing. Soils and Foundations 53, 443–461. https://doi.org/10.1016/J.SANDF.2013.04.006

Kendrick, J.E., Lavallée, Y., Ferk, A., Perugini, D., Leonhardt, R., Dingwell, D.B., 2012. Extreme frictional processes in the volcanic conduit of Mount St. Helens (USA) during the 2004–2008 eruption. Journal of Structural Geology 38, 61–76. https://doi.org/10.1016/j.jsg.2011.10.003

Kendrick, J.E., Lavallée, Y., Hirose, T., Di Toro, G., Hornby, A.J., De Angelis, S., Dingwell, D.B., 2014. Volcanic drumbeat seismicity caused by stick-slip motion and magmatic frictional melting. Nature Geosci 7, 438–442. https://doi.org/10.1038/ngeo2146 http://www.nature.com/ngeo/journal/v7/n6/abs/ngeo2146.html#supplementary-information

Kirkpatrick, J.D., Rowe, C.D., 2013. Disappearing ink: How pseudotachylytes are lost from the rock record. Journal of Structural Geology 52, 183–198. https://doi.org/10.1016/J.JSG.2013.03.003

Klein, J., Mueller, S.P., Castro, J.M., 2017. The Influence of Crystal Size Distributions on the Rheology of Magmas: New Insights From Analog Experiments. Geochemistry, Geophysics, Geosystems 18, 4055–4073. https://doi.org/10.1002/2017GC007114

Lagmay, A.M.F., van Wyk de Vries, B., Kerle, N., Pyle, D.M., 2000. Volcano instability

978 induced by strike-slip faulting. Bulletin of Volcanology 62, 331–346.
979 https://doi.org/10.1007/s004450000103

980 Lavallée, Y., de Silva, S.L., Salas, G., Byrnes, J.M., 2009. Structural control on volcanism at the
981 Ubinas, Huaynaputina, and Ticsani Volcanic Group (UHTVG), southern Peru. Journal of
982 Volcanology and Geothermal Research 186, 253–264.
983 https://doi.org/10.1016/J.JVOLGEORES.2009.07.003

984 Lavallée, Y., Hess, K.U., Cordonnier, B., Dingwell, D.B., 2007. Non-Newtonian rheological law
985 for highly crystalline dome lavas. Geology 35, 843–846.

986 Lavallée, Y., Hirose, T., Kendrick, J.E., Hess, K.-U., Dingwell, D.B., 2015. Fault rheology
987 beyond frictional melting. Proceedings of the National Academy of Sciences 112.

988 Lavallée, Y., Mitchell, T.M., Heap, M.J., Vasseur, J., Hess, K.-U., Hirose, T., Dingwell, D.B.,
989 2012. Experimental generation of volcanic pseudotachylytes: Constraining rheology.
990 Journal of Structural Geology 38, 222–233. https://doi.org/10.1016/j.jsg.2012.02.001

991 Lebti, P.P., Thouret, J.-C., Wörner, G., Fornari, M., 2006. Neogene and Quaternary ignimbrites
992 in the area of Arequipa, Southern Peru: Stratigraphical and petrological correlations.
993 Journal of Volcanology and Geothermal Research 154, 251–275.
994 https://doi.org/https://doi.org/10.1016/j.jvolgeores.2006.02.014

995 Legros, F., 2002. The mobility of long-runout landslides. Engineering Geology 63, 301–331.
996 https://doi.org/10.1016/S0013-7952(01)00090-4

997 Legros, F., Cantagrel, J., Devouard, B., 2000. Pseudotachylyte (Frictionite) at the Base of the
998 Arequipa Volcanic Landslide Deposit (Peru): Implications for Emplacement Mechanisms.
999 The Journal of Geology 108, 601–611. https://doi.org/doi:10.1086/314421

1000 Lin, A., Chen, A., Liau, C.-F., Lee, C.-T., Lin, C.-C., Lin, P.-S., Wen, S.-C., Ouchi, T., 2001.

1001 Frictional fusion due to coseismic landsliding during the 1999 Chi-Chi (Taiwan) ML 7.3
1002 Earthquake. Geophysical Research Letters 28, 4011–4014.
1003 https://doi.org/10.1029/2001GL013253

1004 Lin, A.M., Shimamoto, T., 1998. Selective melting processes as inferred from experimentally
1005 generated pseudotachylytes. JOURNAL OF ASIAN EARTH SCIENCES 16, 533–545.
1006 https://doi.org/10.1016/S0743-9547(98)00040-3

1007 Lipman, P.W., Mullineaux, D.R., 1981. The 1980 eruptions of Mount St. Helens, Washington,
1008 Professional Paper. https://doi.org/10.3133/pp1250

1009 Lucchitta, B.K., 1987. Valles Marineris, Mars: Wet debris flows and ground ice. Icarus 72, 411–
1010 429. https://doi.org/10.1016/0019-1035(87)90183-7

1011 Magloughlin, J.F., 2011. Bubble Collapse Structure: A Microstructural Record of Fluids, Bubble
1012 Formation and Collapse, and Mineralization in Pseudotachylyte. The Journal of Geology
1013 119, 351–371. https://doi.org/10.1086/659143

1014 Magloughlin, J.F., Spray, J.G., 1992. Frictional melting processes and products in geological
1015 materials: introduction and discussion. Tectonophysics 204, 197–204.
1016 https://doi.org/10.1016/0040-1951(92)90307-R

1017 Masch, L., Wenk, H.R., Preuss, E., 1985. Electron microscopy study of hyalomylonites—
1018 evidence for frictional melting in landslides. Tectonophysics 115, 131–160.
1019 https://doi.org/10.1016/0040-1951(85)90103-9

1020 McGuire, W.J., 1996. Volcano instability: a review of contemporary themes. Geological Society,
1021 London, Special Publications 110, 1–23.

1022 Melosh, H.J., 1986. The physics of very large landslides. Acta Mechanica 64, 89–99.
1023 https://doi.org/10.1007/BF01180100

1024 Melosh, H.J., 1979. Acoustic fluidization: A new geologic process? Journal of Geophysical
1025 Research: Solid Earth 84, 7513–7520. https://doi.org/10.1029/JB084iB13p07513

1026 Mueller, S., Llewellin, E.W., Mader, H.M., 2010. The rheology of suspensions of solid particles.
1027 Proceedings of the Royal Society A: Mathematical, Physical and Engineering Sciences 466,
1028 1201–1228. https://doi.org/10.1098/rspa.2009.0445

1029 Nielsen, S., Di Toro, G., Hirose, T., Shimamoto, T., 2008. Frictional Melt and Seismic Slip.
1030 Journal of Geophysical Research: Solid Earth 113, B01308.
1031 https://doi.org/doi:10.1029/2007JB005122.

1032 Nielsen, S., Mosca, P., Giberti, G., Di Toro, G., Hirose, T., Shimamoto, T., 2010. On the
1033 transient behavior of frictional melt during seismic slip. Journal of Geophysical Research-
1034 Solid Earth 115, 17. https://doi.org/B1030110.1029/2009jb007020

1035 Phan, S.-E., Russel, W.B., Zhu, J., Chaikin, P.M., 1998. Effects of polydispersity on hard sphere
1036 crystals. The Journal of Chemical Physics 108, 9789–9795.
1037 https://doi.org/10.1063/1.476453

1038 Reid, M.E., 2004. Massive collapse of volcano edifices triggered by hydrothermal
1039 pressurization. Geology 32, 373–376. https://doi.org/10.1130/G20300.1

1040 Scheidegger, A.E., 1973. On the prediction of the reach and velocity of catastrophic landslides.
1041 Rock Mechanics 5, 231–236. https://doi.org/10.1007/BF01301796

1042 Schneider, C.A., Rasband, W.S., Eliceiri, K.W., 2012. NIH Image to ImageJ: 25 years of image
1043 analysis. Nature Methods 9, 671–675. https://doi.org/10.1038/nmeth.2089

1044 Shea, T., van Wyk de Vries, B., 2008. Structural analysis and analogue modeling of the
1045 kinematics and dynamics of rockslide avalanchesShea and van Wyk de Vries. Geosphere 4,
1046 657–686. https://doi.org/10.1130/GES00131.1

1047 Shimamoto, T., Lin, A., 1994. Is frictional melting equilibrium melting or non-equilibrium
1048 melting? Struct. Geol. (J. Tect. Res. Gro. Japan) 39, 79–84.

1049 Shreve, R.L., 1968. The Blackhawk Landslide. In: Shreve, R.L. (Ed.), The Blackhawk
1050 Landslide. Geological Society of America, 0. https://doi.org/10.1130/SPE108-p1

1051 Sibson, R.H., 1977. Fault rocks and fault mechanisms. Journal of the Geological Society 133,
1052 191–213. https://doi.org/10.1144/gsjgs.133.3.0191

1053 Sibson, R.H., 1975. Generation of Pseudotachylyte by Ancient Seismic Faulting. Geophysical
1054 Journal of the Royal Astronomical Society 43, 775–794. https://doi.org/10.1111/j.1365-
1055 246X.1975.tb06195.x

1056 Siebert, L., 1992. Threats from debris avalanches. Nature 356, 658–659.
1057 https://doi.org/10.1038/356658a0

1058 Siebert, L., 1984. Large volcanic debris avalanches: Characteristics of source areas, deposits,
1059 and associated eruptions. Journal of Volcanology and Geothermal Research 22, 163–197.
1060 https://doi.org/10.1016/0377-0273(84)90002-7

1061 Siebert, L., Glicken, H., Ui, T., 1987. Volcanic hazards from Bezymianny- and Bandai-type
1062 eruptions. Bulletin of Volcanology 49, 435–459. https://doi.org/10.1007/BF01046635

1063 Spray, J., 2010. Frictional Melting Processes in Planetary Materials: From Hypervelocity Impact
1064 to Earthquakes. Annu. Rev. Earth Planet. Sci 38, 221–254.
1065 https://doi.org/10.1146/annurev.earth.031208.100045

1066 Spray, J.G., 1992. A physical basis for the frictional melting of some rock-forming minerals.
1067 Tectonophysics 204, 205–221. https://doi.org/10.1016/0040-1951(92)90308-S

1068 Swanson, D.A., Duffield, W.A., Fiske, R.S., 1976. Displacement of the south flank of Kilauea
1069 Volcano; the result of forceful intrusion of magma into the rift zones, Professional Paper.

https://doi.org/10.3133/pp963

Thouret, J.-C., Finizola, A., Fornari, M., Legeley-Padovani, A., Suni, J., Frechen, M., 2001. Geology of El Misti volcano near the city of Arequipa, Peru. GSA Bulletin 113, 1593–1610. https://doi.org/10.1130/0016-7606(2001)113<1593:GOEMVN>2.0.CO;2

Truby, J.M., Mueller, S.P., Llewellin, E.W., Mader, H.M., 2015. The rheology of three-phase suspensions at low bubble capillary number. Proceedings of the Royal Society A: Mathematical, Physical and Engineering Sciences 471, 20140557. https://doi.org/10.1098/rspa.2014.0557

Violay, M., Di Toro, G., Gibert, B., Nielsen, S., Spagnuolo, E., Del Gaudio, P., Azais, P., Scarlato, P.G., 2014. Effect of glass on the frictional behavior of basalts at seismic slip rates. Geophysical Research Letters 41, 348–355. https://doi.org/10.1002/2013GL058601

Voight, B., 2000. Structural stability of andesite volcanoes and lava domes. Philosophical Transactions of the Royal Society of London 358, 1663–1703.

Voight, B., Elsworth, D., 1997. Failure of volcano slopes. Géotechnique 47, 1–31. https://doi.org/10.1680/geot.1997.47.1.1

Wallace, P.A., De Angelis, S.H., Hornby, A.J., Kendrick, J.E., Clesham, S., von Aulock, F.W., Hughes, A., Utley, J.E.P., Hirose, T., Dingwell, D.B., Lavallée, Y., 2019. Frictional melt homogenisation during fault slip: Geochemical, textural and rheological fingerprints. Geochimica et Cosmochimica Acta 255, 265–288. https://doi.org/10.1016/J.GCA.2019.04.010

Wang, Y.F., Dong, J.J., Cheng, Q.G., 2017. Velocity-dependent frictional weakening of large rock avalanche basal facies: Implications for rock avalanche hypermobility? Journal of Geophysical Research: Solid Earth 122, 1648–1676. https://doi.org/10.1002/2016JB013624

Webb, S.L., Dingwell, D.B., 1990. The onset of non-Newtonian rheology of silicate melts. Physics and Chemistry of Minerals 17, 125–132. https://doi.org/10.1007/BF00199663

Weidinger, J.T., Korup, O., 2009. Frictionite as evidence for a large Late Quaternary rockslide near Kanchenjunga, Sikkim Himalayas, India — Implications for extreme events in mountain relief destruction. Geomorphology 103, 57–65. https://doi.org/10.1016/J.GEOMORPH.2007.10.021

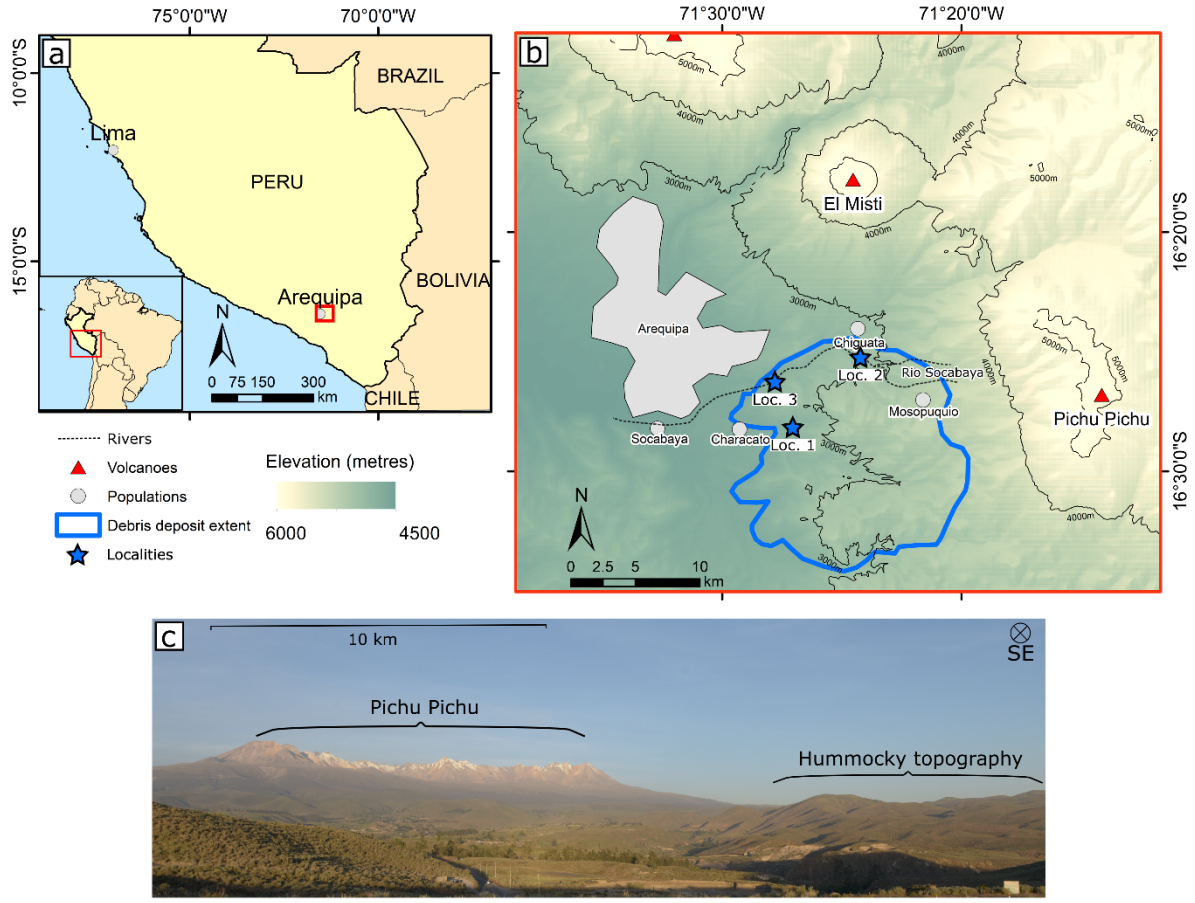


Figure 1. Locality map and field photos to illustrate debris avalanche deposit and source location. a) Map of southern Peru (red box marks area in b) with inset of South America (red box shows the map area). b) Topographic map of the Arequipa basin, Pichu Pichu, the debris avalanche deposit (blue outline) and field localities for this study (Loc. 1-3). c) Photo of dissected Pichu Pichu arcuate ridge and the debris avalanche deposit showing raised humocky topography, view is SE from Chiguata.

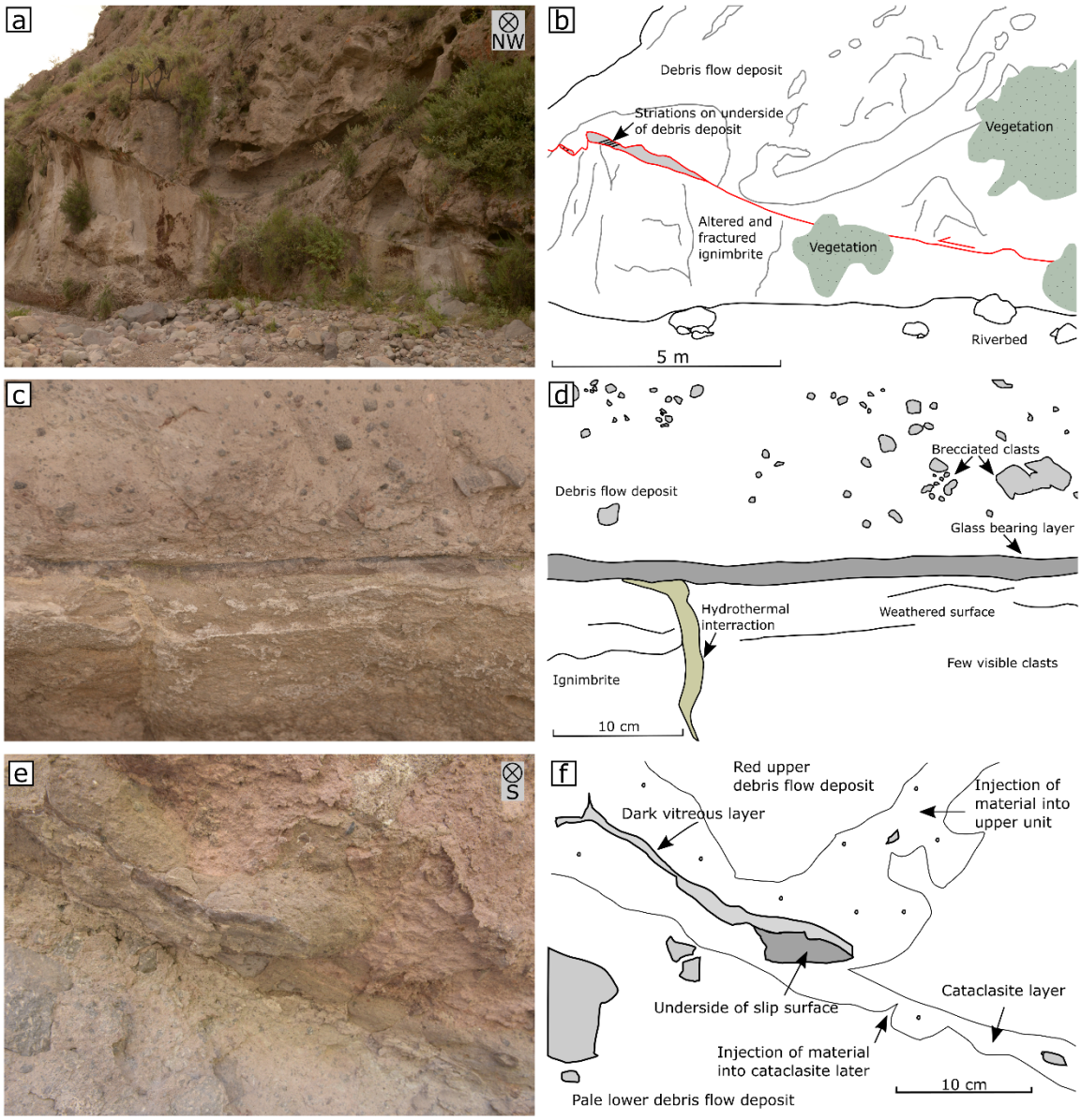


Figure 2. Field photos and sketches of features at Locality 1. a-b) Basal contact of the debris flow with basal topology leading to extreme shear localisation. c-d) Close view of the basal surface with localised dark, vitreous, glass-bearing layer. e-f) Secondary shear zone 20 m above the outcrop in panels a-d showing juxtaposition of units separated by cataclasite plus a dark, vitreous seam.

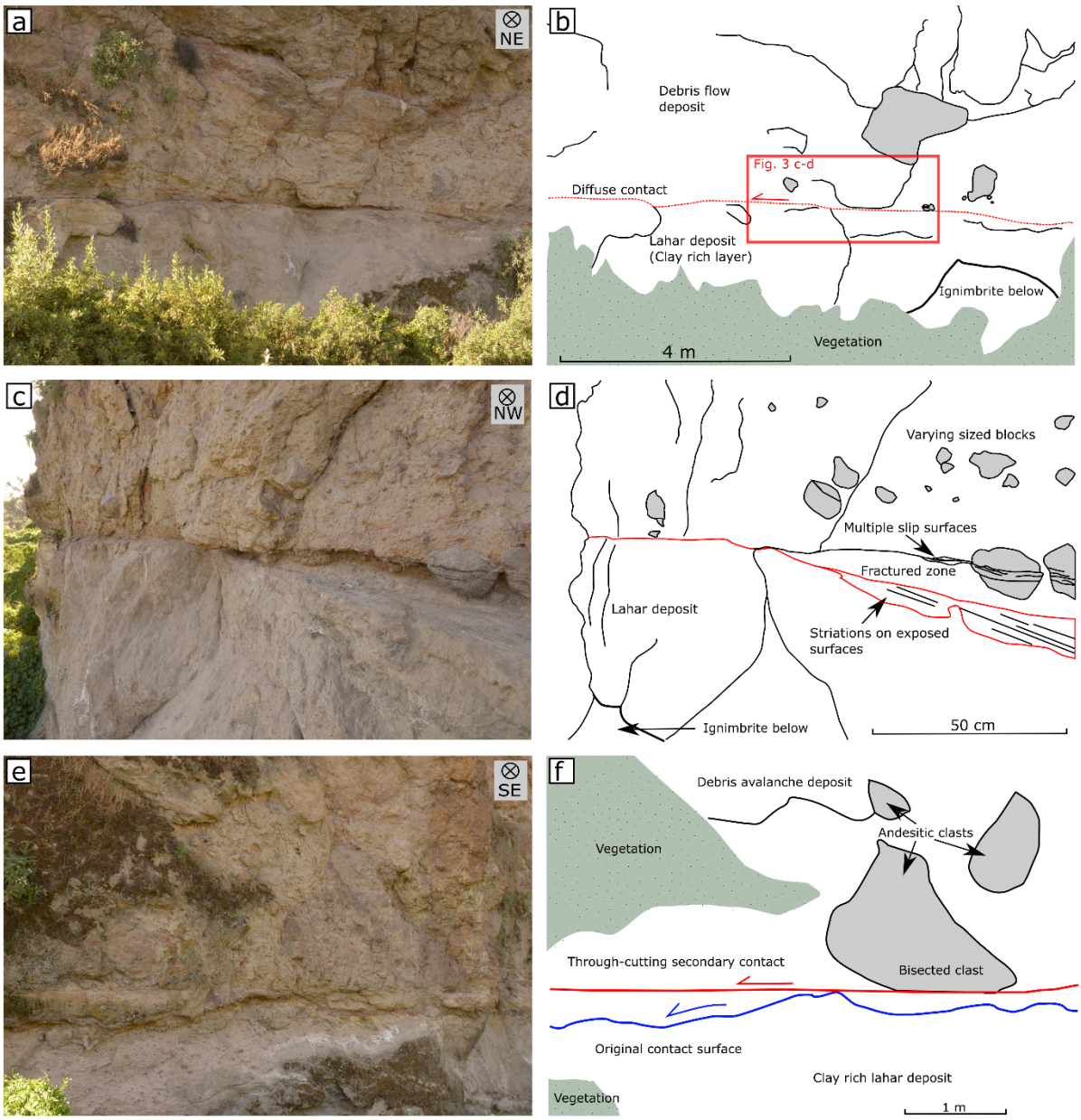


Figure 3. Field photos and sketches from Locality 2. a-b) Debris avalanche deposit with large clasts and 40 cm thick diffuse basal contact. c-d) Closer view showing intense fracturing and cataclasis along the slip zone, multiple fractures cutting andesitic blocks in the fractured zone marked and striations on the lower slip surface. e-f) Basal contact 140 m west (downstream) showing how rough topology of the original contact (blue) is superseded by a secondary through-cutting contact (red) that also bisects a clast.

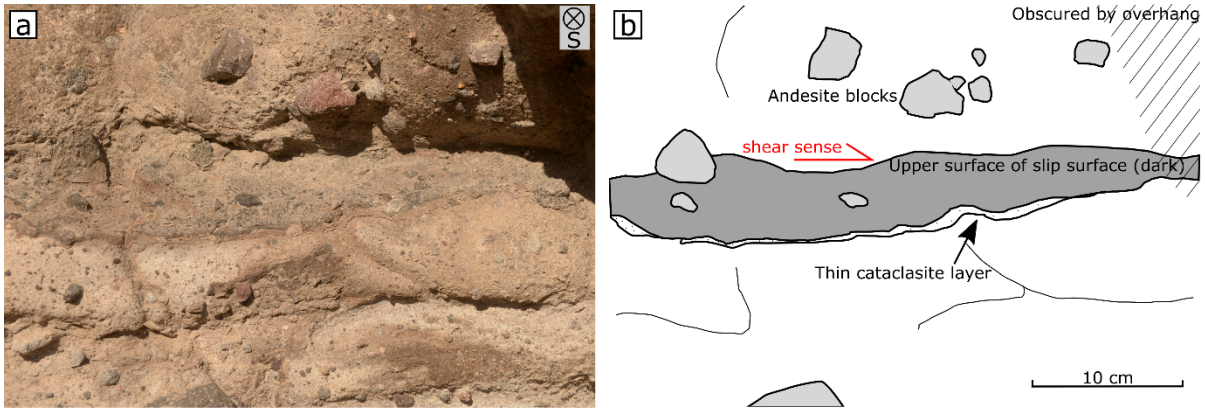


Figure 4. Field photo and sketch of a secondary shear surface within the debris avalanche at Locality 3 bounded by a thin layer of very fine cataclasite. The outcrop is oblique to vertical, revealing the top surface of the cataclastic vein. Moderately large clasts and blocks are present either side of the boundary, with shear indicators largely absent.

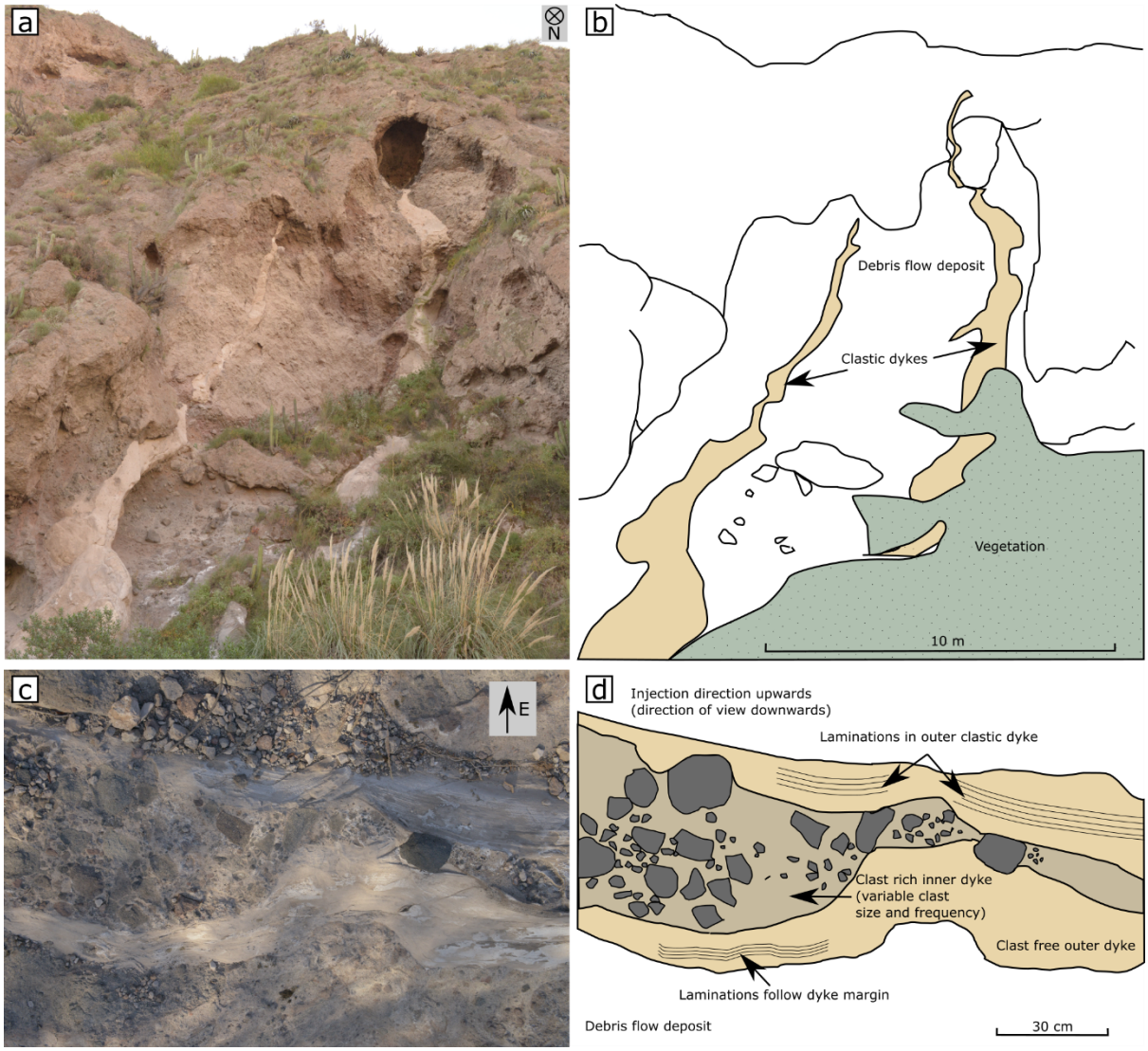


Figure 5. Field photos and sketches of Locality 3. a-b) Clastic dykes with variable thickness (0.05-1.5 m) injected up to 20 m sub-vertically into the debris avalanche deposit with sharp, undulating boundaries. c-d) Clast rich (primarily andesitic) clastic dyke located 80 m east of that shown in a-b, with larger clasts in the centre and a fine grained boundary. The direction of injection is upwards.

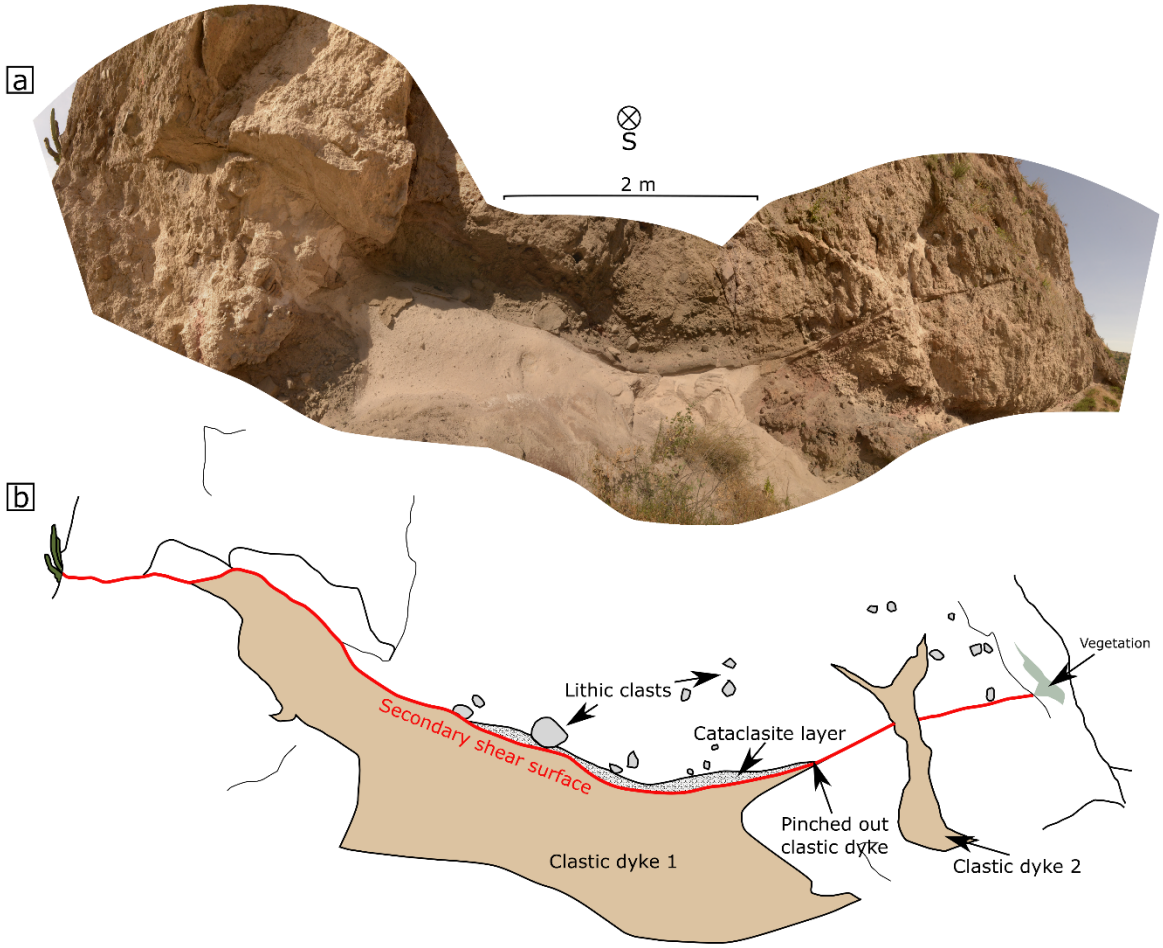


Figure 6. Stitched panoramic field photo and sketch of secondary shear surface interaction with clastic dyking at Locality 3. A large clastic dyke initiated from the primary basal slip surface below (not shown) terminating at the linear secondary shear surface feature in the outcrop. A second clastic dyke to the right of the image cross-cuts this linear feature with no displacement.

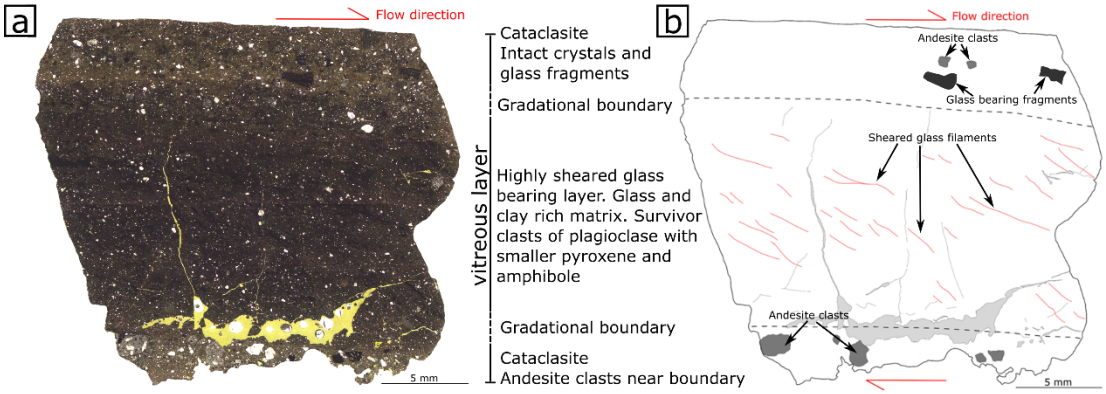


Figure 7. Thin section photomicrograph (in plane polarised light) showing the full thickness of the glass-bearing basal layer from Loc. 1. The layer is bounded by cataclasite and separates andesitic debris avalanche deposit above and the ignimbrite below (not shown here). A dark, glass bearing central layer contains sheared glass filaments (black areas, annotated with red lines in sketch), ultracataclasite (brown areas) and survivor clasts. The bounding cataclasite contains coarser crystal, lithic and relict melt fragments (thin section PPA1_1.1).

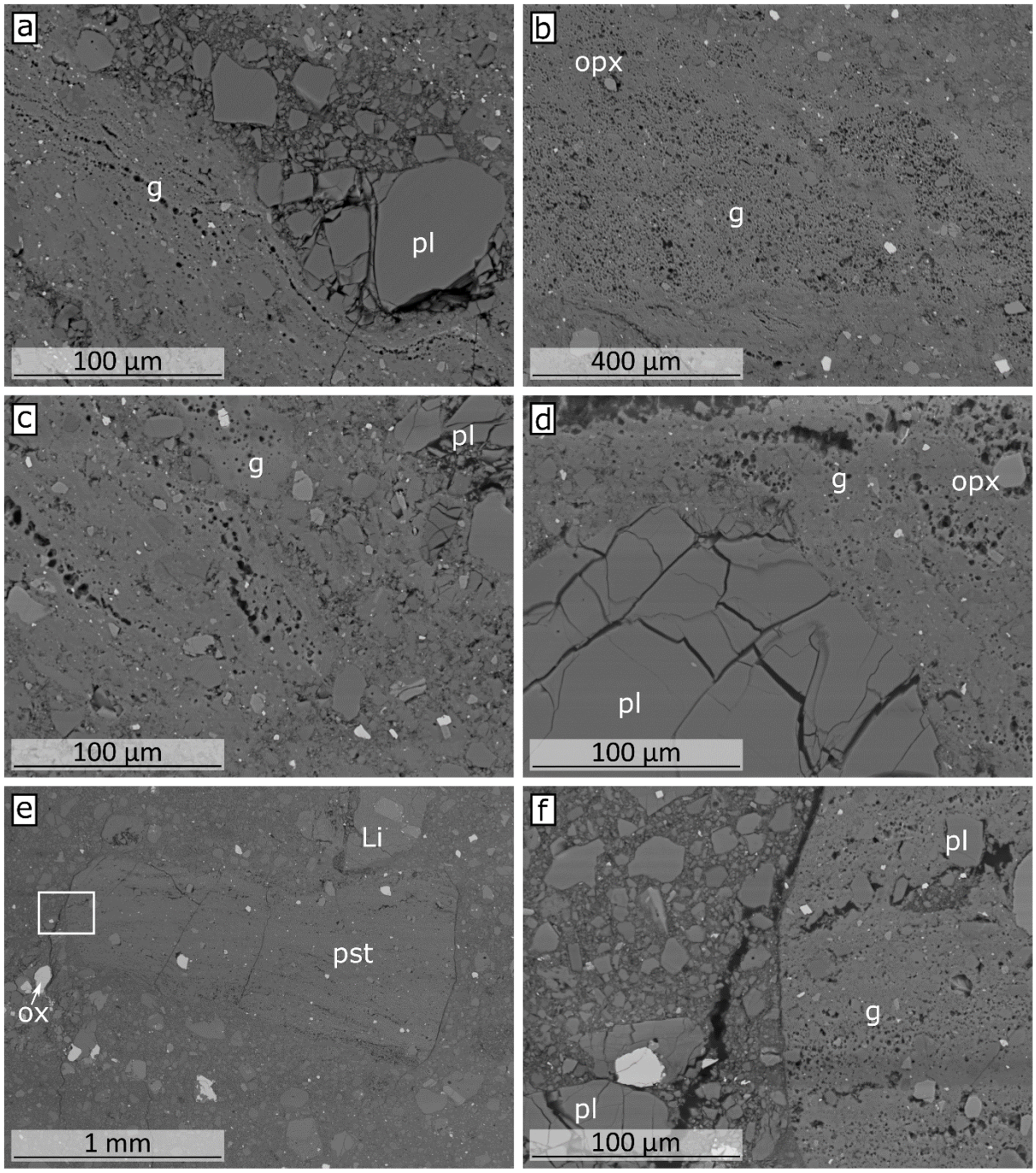


Figure 8. BSE images of the vitreous basal layer from Loc. 1 (also shown in Fig. 7). a) A sheared and fractured plagioclase clast within the glass-bearing layer. b) Vesicular glass in the primary slip surface with stretched bubbles along the lower boundary indicating shear. c) Sheared and vesicular glass and ultracataclasite, following Riedel shear directions. d) Fractured plagioclase survivor clast within the preserved glass bearing layer. e) Glass-bearing pseudotachylyte fragment within the cataclasite (box shows position of f). f) The rounded margin of the pseudotachylyte fragment with intermixed layers of ultracataclasite and glass, within the granular cataclasite. pl=plagioclase, g=glass, ox=oxides, opx=orthopyroxene, Li=lithic clast, pst=pseudotachylyte clast (thin section PPA1_1.1).

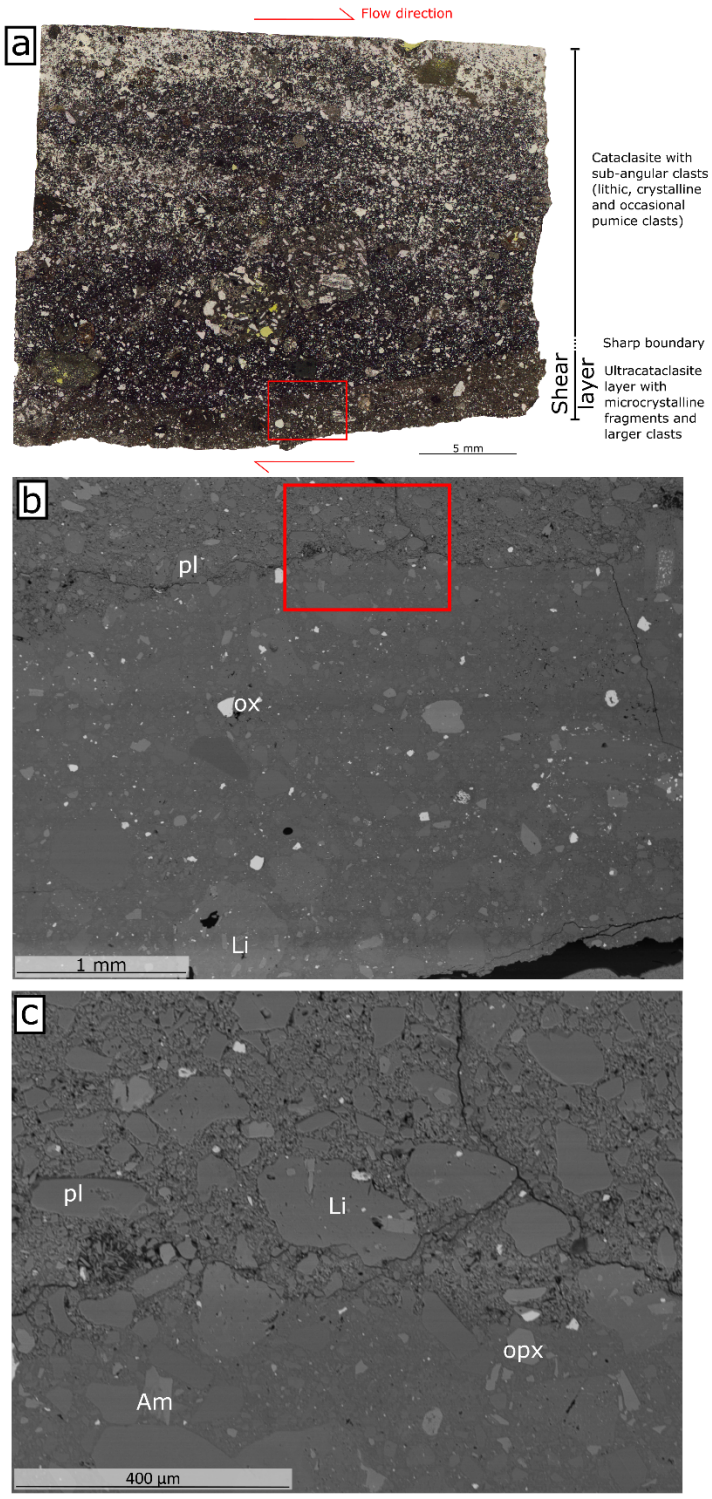


Figure 9. Thin section from secondary slip surface at Loc. 1. a) A PPL photomicrograph showing cataclastic textures (clasts >0.5 mm) with darker brown ultracataclasite making up the primary shear layer at the base (red box shows area in b). b) BSE image of the granular cataclasite above the denser ultracataclasite (red box shows area in c). c) The cataclasite and ultracataclasite show similar components (crystal and lithic clasts) but are distinguished by an abrupt porosity contrast (thin section PPA1_5.3).

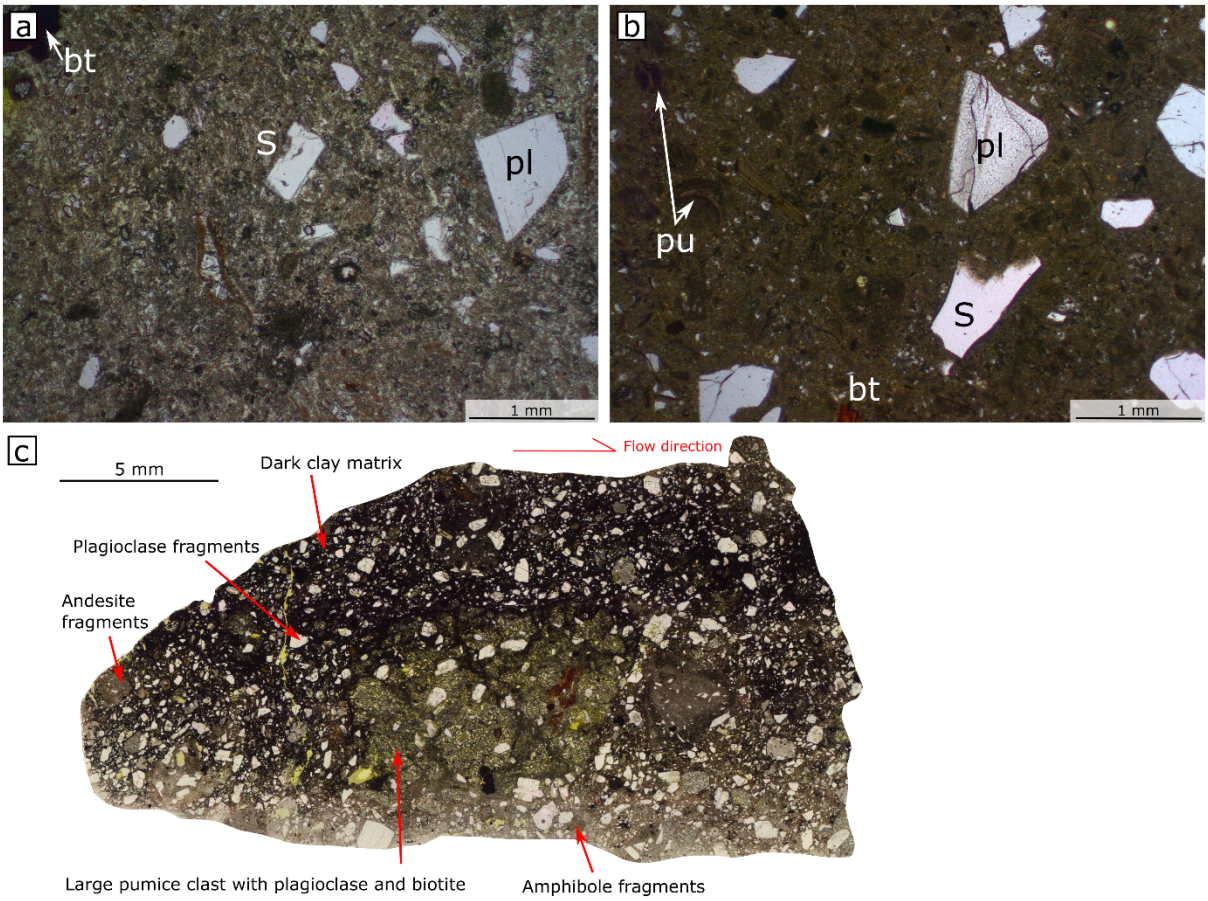


Figure 10. PPL photomicrographs illustrating mineralogy of a) Porous ignimbrite from Loc. 1 with sanidine (S), plagioclase (pl) and biotite (bt) crystals in a glass shard matrix (thin section PPA1_1.1). b) Clastic dyke from Loc. 3 with sanidine, plagioclase, biotite and pumice (pu) shards with high clay content in the matrix (thin section PPA2_2.1). c) The cataclastic basal shear zone at Loc. 2 hosts a range of clasts of different size and composition (thin section PPA3_2.1).

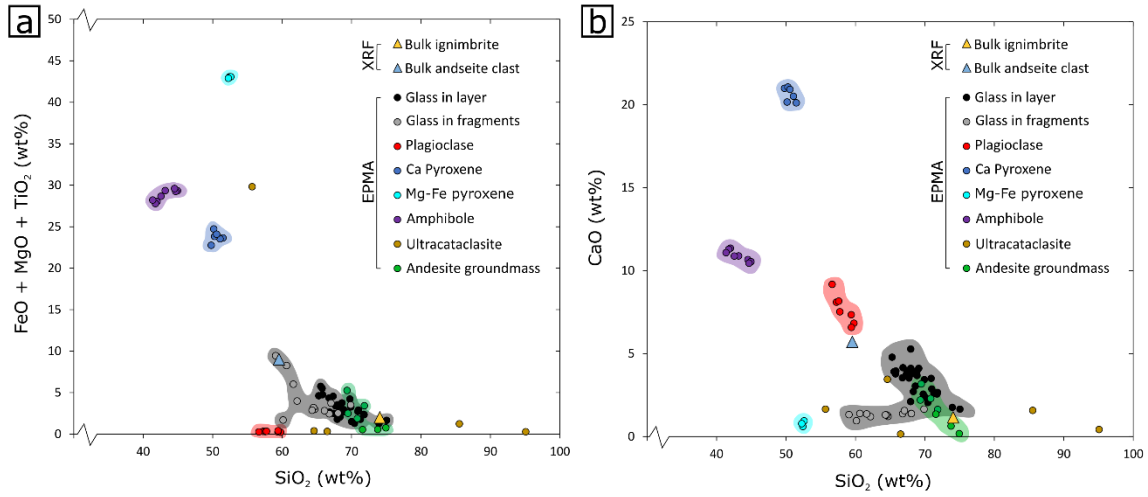


Figure 11. Chemical analyses by XRF (triangles) of an andesite clast from the debris avalanche and ignimbrite from Loc. 1, and chemical analyses by EPMA of the glass within the pseudotachylyte layer from Loc. 1, as well as plagioclase, amphibole, pyroxene and the groundmass from 3 andesite clasts and plagioclase and biotite from the ignimbrite, plotted as: a) Mafic ($FeO + MgO + TiO_2$) wt.% against silicon dioxide ($SiO_2$) wt.% showing relation of frictional melt (glass) to bulk chemistry and individual minerals; and b) Calcium oxide (CaO) wt% against $SiO_2$ wt%, with low CaO wt% suggesting involvement of andesitic enstatite (Mg-Fe pyroxene) in generation of the fragmented glass.

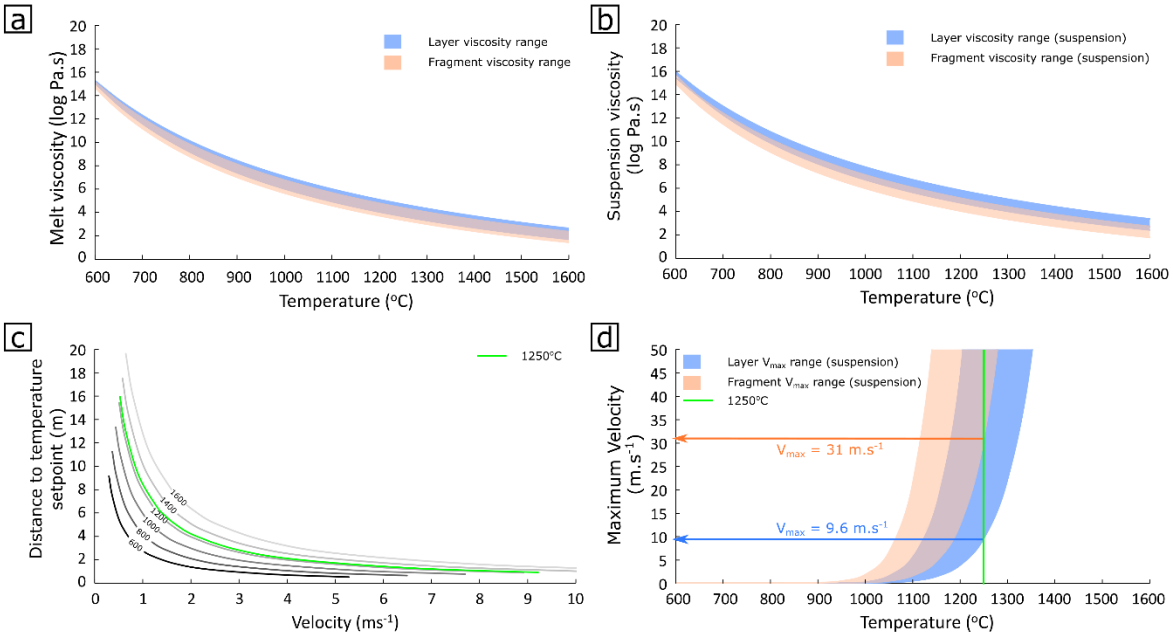


Figure 12. Modelling the generation and rheology of the frictional melts. a) Temperature-viscosity relationships of the glass in the preserved layer (blue) and fragment (orange), using Eqs. 1-2. b) Temperature-viscosity relationships of the preserved layer and fragment considering the suspended solid fraction and bubbles, using Eq. 9. c) Slip distance required to produce heating of a given magnitude (contours) for different slip velocities, using Eq.3, showing the estimated maximum temperature, 1250 °C (green). d) Maximum possible velocity experienced by the modelled suspensions avoiding brittle failure. Presence of fragments suggests velocity exceeded 31 $ms^{-1}$ at 1250 °C and melting persisted to form the preserved layer.

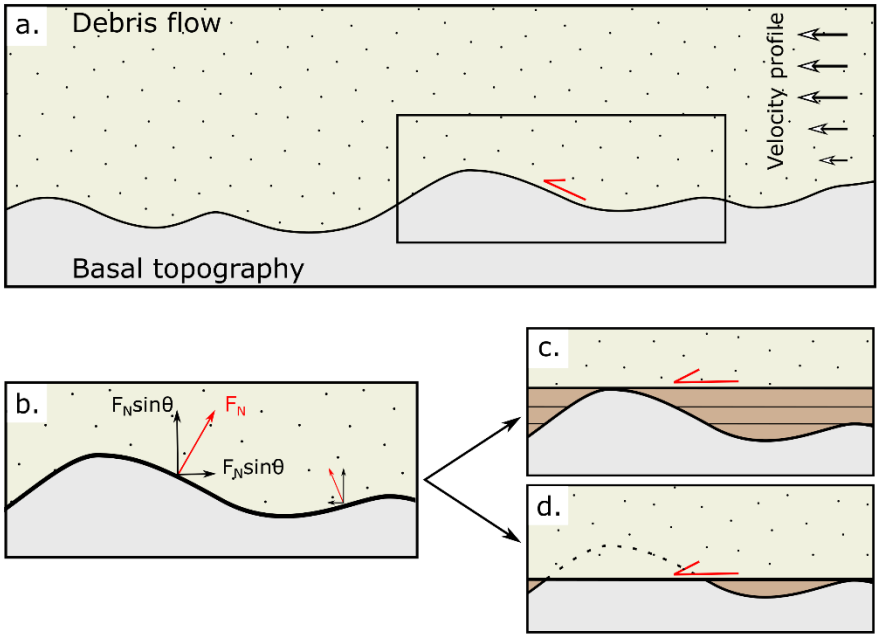


Figure 13. Sketch diagrams illustrating successive shear localisation by rupture or asperity ploughing (may occur at a range of scales). a) A rough surface with velocity profile (indicated by arrow size). b) A rough surface influencing normal, compressive force ($F_N$) induced by topography. c) Scenario 1, faster moving upper flow propagates along a newly formed shear surface. d) Scenario 2, an asperity is removed by fracturing and is incorporated into the flow.

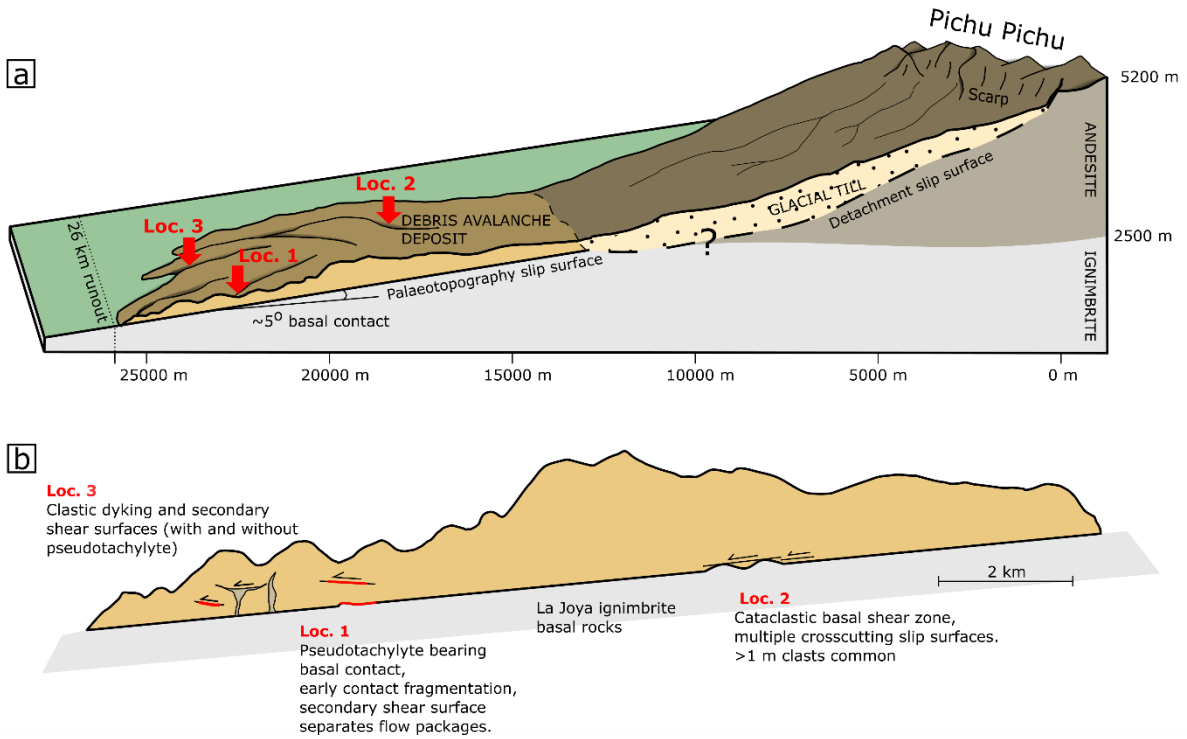


Figure 14. Sketches outlining preserved processes in the Pichu Pichu debris avalanche deposit. a) Scaled sketch illustrating deposit, source and studied outcrops in this study. b) Flattened idealised cross section of features of the flow interior (topography scale increased by factor of 2 and features not to scale) summarising the observations of the field study and variation in basal shear zone morphology.

Table 1. Values for variables A, B and C used to determine melt viscosity with Eq. 1 and 2. Min and max represent compositional ranges from low to high (respectively) $SiO_2$ concentration of the glass-bearing layer and fragment. The values of A, B and C are used to constrain the viscosity of each frictional melt ($\eta$) and apparent viscosity of each suspension (at a strain rate of $10^3$ $s^{-1}$) at a nominal temperature of 1250 ˚C.

| | A | | B | | C | | $log\eta$ at 1250 ˚C | | $log\eta_{app}$ | |
|---|---|---|---|---|---|---|---|---|---|---|
| Sample | Min | Max | Min | Max | Min | Max | Min | Max | Min | Max |
| Layer | -4.55 | -4.55 | 9126.4 | 11264.3 | 406.7 | 304.8 | 3.62 | 4.69 | 4.34 | 5.42 |
| Fragment | -4.55 | -4.55 | 8681.8 | 10666.0 | 421.2 | 332.4 | 3.33 | 4.41 | 3.67 | 4.75 |

Supplementary material

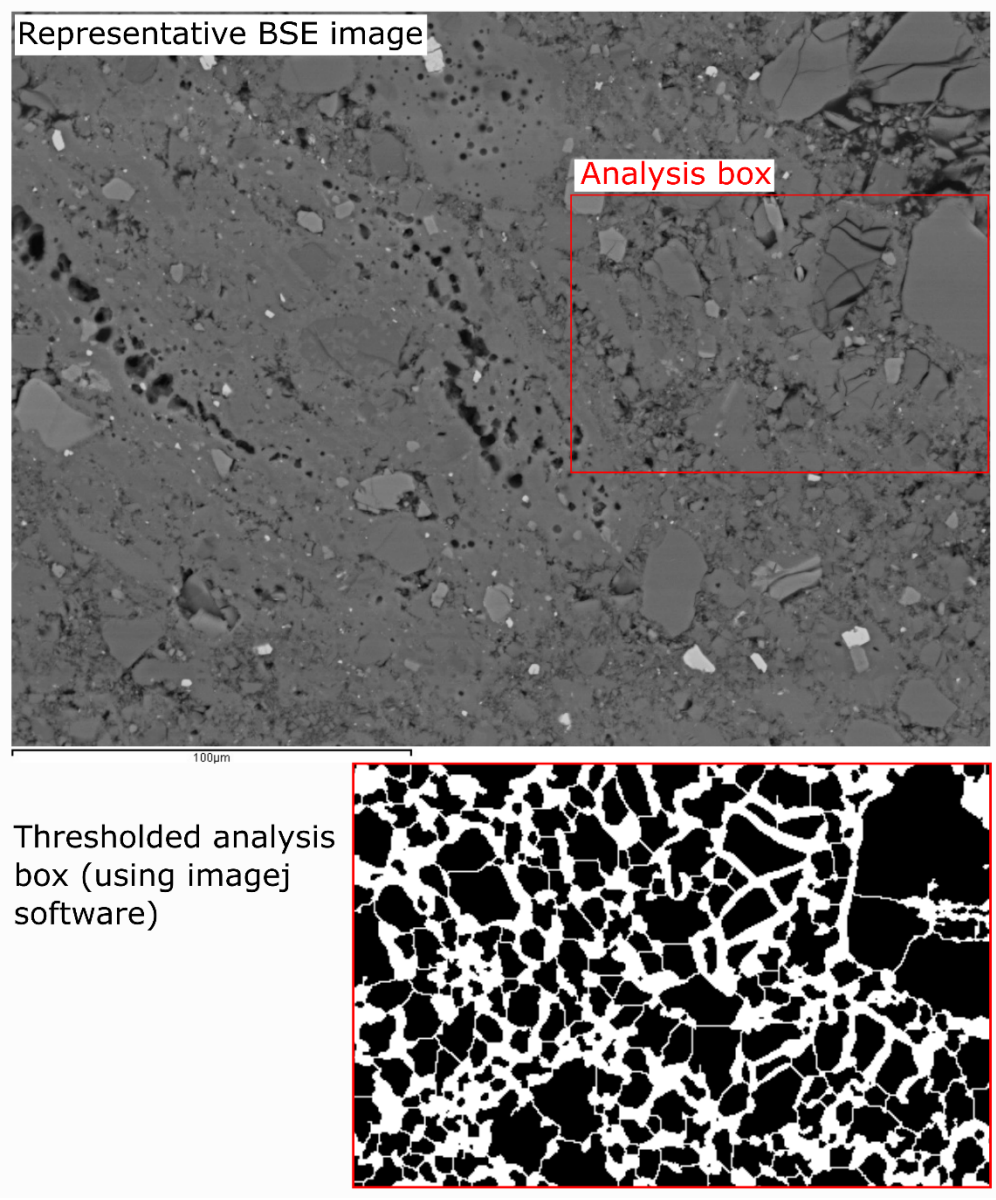


Supplementary figure 1. a) Representative BSE image from basal layer at Locality 1. (See Figure 8). Red box shows area of analysis. b) Image of thresholding output from ImageJ software. Each black section is identified as a separate particle from which area, perimeter, major and minor axis length, circularity and aspect ratio are measured (see supplementary files for dataset).